Journal of
Marine Science and Engineering

MDPI

Article

Integrated 1D Simulation of Aftertreatment System and Chemistry-Based Multizone RCCI Combustion for Optimal Performance with Methane Oxidation Catalyst

Alireza Kakoee [1,*], Jacek Hunicz [2] and Maciej Mikulski [1,3]

[1] School of Technology and Innovation, University of Vaasa, Yliopistonranta 10, 65200 Vaasa, Finland; maciej.mikulski@uwasa.fi
[2] Faculty of Mechanical Engineering, Lublin University of Technology, Nadbystrzycka 36, 20-618 Lublin, Poland; j.hunicz@pollub.pl
[3] Vaasa Energy Business and Innovation Center (VEBIC), Yliopistonranta 3, 65200 Vaasa, Finland
* Correspondence: alireza.kakoee@uwasa.fi

Abstract: This paper presents a comprehensive investigation into the design of a methane oxidation catalyst aftertreatment system specifically tailored for the Wärtsilä W31DF natural gas engine which has been converted to a reactivity-controlled compression ignition NG/Diesel engine. A GT-Power model was coupled with a predictive physical base chemical kinetic multizone model (MZM) as a combustion object. In this MZM simulation, a set of 54 species and 269 reactions as chemical kinetic mechanism were used for modelling combustion and emissions. Aftertreatment simulations were conducted using a 1D air-path model in the same GT-Power model, integrated with a chemical kinetic model featuring 15 catalytic reactions, based on activation energy and species concentrations from combustion outputs. The latter offered detailed exhaust composition and exhaust thermodynamic data under specific operating conditions, effectively capturing the intricate interactions between the investigated aftertreatment system, combustion, and exhaust composition. Special emphasis was placed on the formation of intermediate hydrocarbons such as C_2H_4 and C_2H_6, despite their concentrations being lower than that of CH_4. The analysis of catalytic conversion focused on key species, including H_2O, CO_2, CO, CH_4, C_2H_4, and C_2H_6, examining their interactions. After consideration of thermal management and pressure drop, a practical choice of a 400 mm long catalyst with a density of 10 cells per cm^2 was selected. Investigations of this catalyst's specification revealed complete CO conversion and a minimum of 89% hydrocarbon conversion efficiency. Integrating the exhaust aftertreatment system into the air path resulted in a reduction in engine-indicated efficiency by up to 2.65% but did not affect in-cylinder combustion.

Keywords: aftertreatment; MOC; hydrocarbons; combustion; multizone model; chemical kinetics; emissions; engine

Citation: Kakoee, A.; Hunicz, J.; Mikulski, M. Integrated 1D Simulation of Aftertreatment System and Chemistry-Based Multizone RCCI Combustion for Optimal Performance with Methane Oxidation Catalyst. *J. Mar. Sci. Eng.* **2024**, *12*, 594. https://doi.org/10.3390/jmse12040594

Academic Editors: Tie Li and Xinyi Zhou

Received: 3 March 2024
Revised: 26 March 2024
Accepted: 28 March 2024
Published: 29 March 2024

1. Introduction

Despite the increasing role of electrification in automotive powertrains, marine and off-road applications are expected to continue relying on internal combustion engines for the foreseeable future. This is due to their unique operational requirements, such as high torque demand, long operating hours, packaging constraints, and limited access to refuelling infrastructure. Primary challenges for powertrain development in the marine and off-road sectors involve flexible inclusion of low-carbon alternative fuels while improving fuel efficiency and reducing atmospheric emissions [1]. Advanced low-temperature combustion concepts (LTC) are currently at the forefront of developments to meet those challenges. Reactivity-controlled compression ignition (RCCI) in particular is under intense investigation by leading marine engine manufacturers, including Wärtsilä [2] and MAN Energy Solutions [3]. RCCI retains the benefits of conventional dual-fuel ignition, resulting in

improved fuel efficiency, lower emissions of nitrogen oxides (NOx) and particulate matter (PM), and enhanced engine performance in these demanding applications [4–6]. Moreover, RCCI enables gradual integration of green hydrogen or ammonia into existing natural gas infrastructures, combining the simultaneous combustion of different fuels. Keeping the existing infrastructure avoids extensive modifications and reduces environmental impact [7–9].

Due to its lower combustion temperature, an RCCI engine produces more carbon moNOxide (CO) and hydrocarbon (HC) emissions than a conventional diesel engine [10]. For example, Benajes et al. [11] performed dynamic emission tests to compare emissions from a car engine operated in conventional diesel combustion (CDC) and diesel–gasoline RCCI modes. Despite lower PM and NOX production, switching to RCCI mode increased CO and HC engine-out emissions from 7.5 g/kWh to 14.7 g/kWh and from 4.9 g/kWh to 7.9 g/kWh, respectively. Similar emission levels for diesel–gasoline RCCI were shown by Kokjohn et al. [12] for steady engine operation at 0.6 MPa of indicated mean effective pressure (IMEP), namely, 14 g/kWh and 6 g/kWh for CO and HC, respectively. It should be noted that emission levels strongly depend on combustion controls such as diesel injection strategy, fuel fractions, boost, and exhaust gas recirculation (EGR). However, a reduction in CO and HC emissions usually is associated with an increase in NOX emissions [13]. Pedrozo et al. [14] provided emission results for a diesel–natural gas (NG) RCCI engine. At IMEP 0.6 MPa, HC emission levels were similar to other cited works at approximately 6 g/kWh, notably almost completely comprising methane. This unburned methane emission—methane slip—is a potent greenhouse gas contributing to climate change [15]; so, its excessive emission can negate all of the other emission benefits of RCCI combustion. Mortensen et al. [16] calculated that just 3% methane slip completely wastes NG's advantage over coal in terms of greenhouse gas warming potential over a 20-year term.

CO and HC emissions also directly reduce combustion efficiency, so different control approaches have been proposed to reduce these emissions while keeping LTC's PM and NOx emission benefits. Beside fuel-mixing strategies, variable valve timing and variable compression ratio are two technologies that can affect internal combustion engine emissions. Variable valve timing optimises the engine's valve timing, improving combustion efficiency, reducing pumping losses, and enhancing power and torque. This leads to reduced NOx and PM emissions while also enhancing fuel efficiency. A variable compression ratio allows for the adjustment of the engine's compression ratio during operation, thereby optimising combustion based on load and operating conditions. This can lead to more complete combustion while maintaining low NOx emissions [17,18]. Mikulski et al. [6] proposed to adapt in-cylinder fuel reforming from homogenous charge compression ignition (HCCI) technology for RCCI, aiming to reduce methane slip. Although such strategies are used to improve emission control in RCCI engines, using an exhaust aftertreatment system to convert CO and HC is inevitable if further tightening of emission legislation is considered.

Typically, the mitigation of HC and CO emissions in a lean environment involves the use of an oxidation catalyst. Diesel oxidation catalysts (DOCs) are commonly used for oxidising HC and CO in conventional diesel engines. DOCs also improve the efficiency of the diesel particulate filter and selective catalytic reduction [19]. First-generation DOCs with copper (Cu), nickel (Ni), or other metals were based on gasoline engine technology, but they were phased out due to susceptibility to catalyst poisoning and poor thermal stability. The second-generation ones used high loading of noble metals such as platinum (Pt), palladium (Pd), and rhodium (Rh). They gave greater conversion efficiency of CO and HC. However, they have been associated with high sulphate emissions. Third-generation DOC catalysts use HC adsorption technology, with strong HC adsorption materials such as molecular sieves. Most of the HC emissions during the cold start and warm-up stages are adsorbed, and then desorbed and completely burned in the heating stage [20,21]. This solution reduces the necessity of catalyst heating by combustion delay, which reduces the engine's thermal efficiency [22].

LTC's inherent characteristic of low exhaust gas temperature poses a challenge for existing exhaust aftertreatment solutions. Hasan et al. [23–25] studied catalytic efficiency of an HCCI engine aftertreatment system in various studies, reporting indicated low methane conversion efficiency of a standard three-way catalytic converter. The efficiency was as low as 16% at 0.4 MPa IMEP, compared to 92% for spark-ignition combustion. Hunicz and Medina [26] analysed methane oxidation efficiency and, aside from the temperature effect, they pointed out the poisoning effect of acetylene, which is produced by fuel reforming. Prikhodko et al. [27] examined different DOC converters with different loadings and precious metal proportions, working with a diesel–gasoline RCCI engine. The conversion efficiency was 100% for CO and 80% for HC as soon as the exhaust temperature reached 190 °C in CDC operation, independent of the catalytic material. In contrast, the same conversion efficiencies were not achieved until 300 °C in RCCI operation. The differences in catalytic efficiency were ascribed to overall higher concentrations of CO and HC and also to different hydrocarbon compositions.

Considering the above, RCCI with NG as a low-reactivity fuel is particularly challenging due to the high dissociation enthalpy of methane. Therefore, it is difficult to activate the catalytic reaction under the low temperatures that are typical of RCCI exhaust. This indicates that dedicated methane oxidation catalysts (MOCs) should be applied in RCCI engines. An MOC's design, precious metal composition, and sizing play a crucial role in reducing methane emissions. Usually, MOCs are based on Pt and Pd, with Pd showing the highest activity under lean conditions and in a low-temperature regime. Stakheev et al. [28] tested Pt and Pd on aluminium oxide (Al_2O_3) catalysts in lean conditions and with 5000 ppm methane concentration. For the best performing design, a Pt-based catalyst had a light-off temperature of 510 °C, while a Pd-based one had a 360 °C light-off temperature. The Pt catalysts used a Langmuir–Hinshelwood mechanism on metallic Pt, while the Pd catalysts employed a Mars–Van Krevelen mechanism on Pd oxide particles. Pt and Pd catalysts have a different relationship between their activity and metal particle size. Pd catalysts became more active as particle size increased from 1 to 20 nm, while Pt catalysts were mostly unaffected by particle size. These differences stemmed from distinct reaction mechanisms: weaker Pd–O bonds and reduced support effects enhanced the activity of larger Pd particles. Currently, the most investigated type of MOC for large dual-fuel gas engines is Pd on Al_2O_3. However, the newest investigations show advantages of zeolite support [14]. Sulphur poisoning is a particular challenge for state-of-the-art MOCs. According to Ottinger et al. [29], as little as 1 part per million (ppm) of sulphur dioxide (SO_2) in the exhaust inhibits the catalyst. Lehtoranta et al. [30] considered using an upstream SOx trap to mitigate the problem, but the MOC still required 20 h regeneration intervals to keep the methane (CH_4) conversion efficiency above 70%, even with only 0.5 ppm of SO_2 in the exhaust. Importantly, increased concentrations of H_2 in the exhaust can dramatically accelerate regeneration [31].

Pd-MOCs have been relatively well researched for conventional dual-fuel marine engines, but that is not the case for NG–diesel RCCI because of the low TRL level of the combustion concept. Fast, one-dimensional (1D) reactive simulation can be coupled with engine and aftertreatment models for system level simulation to evaluate the feasibility of such a paring. This model-based development method has been widely used in global R&D. Tziolas et al. [32] investigated several close-coupled exhaust aftertreatment system (EATS) layouts aimed at meeting future EURO VII diesel emission limits. The study used a heavily predictive EATS model build in Exothermia Suite but coupled it with a non-predicative, fast-running engine model (GT-Suite) of a diesel engine for fast transient simulations. Such an approach is typical for legacy engines, because neither conventional diesel combustion (CDC) nor spark-ignited (SI) flame propagation is particularly sensitive to intake valve closing (IVC) conditions. Recently, a similar co-simulation approach was used by Leon de Syniawa et al. [33] to develop a comprehensive, detailed kinetic MOC model for SI compressed natural gas (CNG) engines. The baseline for the MOC model was a platinum group metal (PGM) chemistry containing Pt and rhodium (Rh) with Ceria (CeO_2).

Importantly, the authors underscored the value of using a predictive combustion model with detailed chemistry to capture the influence of non-legislative emission components on aftertreatment performance [32]. The modelling assumed indirect coupling of a zero-dimensional (0D) SI stochastic reactor model (SRM) with a 1D catalyst model. Indirect coupling meant only composition of the exhaust was passed to the catalyst brick, while the boundary conditions of intake and exhaust manifold pressure and temperature were imposed in both models directly from the experimental data. At this point, one should note that unlike CDC and SI combustion, the kinetically controlled nature of RCCI combustion makes it very sensitive to IVC conditions. Even small fluctuations in intake and exhaust path include a direct feedback loop in combustion, producing cycle-to-cycle variations in exhaust composition and indicated efficiency. Consequently, inclusion of the MOC brick's backpressure will affect engine-out emissions and efficiency, yielding fully dynamic two-way coupling between the predictive combustion, air path, and aftertreatment. This is a significant methodological challenge, considering that commercial 1D solvers do not offer a fully predictive approach to model RCCI combustion.

2. Motivation and Objectives

Summarising the above state of the art, NG–diesel RCCI offers ultra-low emissions and near-zero NOx and PM emissions and is considered the next big thing for marine propulsion. On the other hand, CH_4 and CO emission levels, although much lower than those of legacy methane-based combustion concepts, still pose a challenge and will require aftertreatment if future emission legislation becomes more stringent. Coupling RCCI with aftertreatment, particularly state-of-the-art MOC, is uncharted territory and contains several knowledge gaps. Some insights suggest that the two technologies might not be complementary. RCCI implies low exhaust temperature and potentially high formaldehyde and nitrous oxide (N_2O) emissions. Sulphur from the diesel fraction used as high-reactivity fuel can still be transferred to the exhaust. These factors inhibit MOC performance. On the other hand, the concept offers potential opportunities. An MOC can reduce RCCI's extensive calibration burden and aftertreatment regeneration can benefit from future H2-NG mixtures that are expected to gradually enter marine bunkering streams.

A predictive 1D simulation framework can be used to resolve this conflict between the challenges and opportunities at an early stage of concept development. The early stage of development of both RCCI and MOC technology for large-bore engines creates a methodological knowledge gap in this respect. To this end, the present work is a step towards developing an integrated methodology capable of predicting the emission and performance characteristics of cutting-edge marine dual-fuel engines working in low-temperature RCCI mode with MOC aftertreatment. To this end, a fully predictive, in-house University of Vaasa advanced thermokinetic multizone (UVATZ) combustion model [34,35] is dynamically coupled with a 1D model (GT-Suite) of a prototype engine built to test RCCI combustion on a representative geometry of Wärtsilä 31DF production engines. The integrated combustion–air-path model has been thoroughly calibrated and further coupled with a representative state-of-the-art MOC catalyst model built in the same GT-Suite environment [36]. The MOC includes a well-established PGM chemistry model created by Khosravi et al. [37], tuned to the detailed exhaust species portfolio of the UVATZ code. This study's primary objective is to determine the feasibility of this unique modelling framework for integrated calibration of RCCI engines with aftertreatment. The objective is achieved by performing steady-state simulations focused on convergence and fundamental cross-interactions of the system's components. With fundamental feasibility confirmed, this study moves on to geometrical optimisation of the MOC and several case studies to support the applied feasibility of the RCCI-MOC system.

3. Methodology

3.1. The Test Engine and the Engine Model

The air-path and combustion models used in this study were identified based on the Wärtsilä Mono single-cylinder research engine (SCRE) platform. The cylinder geometry of the SCRE was selected from Wärtsilä's 310 mm bore, dual-fuel production engine specifications. Table 1 lists the main specifications of the test rig. The same engine, running low-temperature RCCI combustion, has provided data for model validation.

Table 1. Specifications of the Wärtsilä Mono single-cylinder research engine.

Displacement and nominal speed	32.45 L/720 rpm
Stroke/bore	1.39:1
Air system	External air compressor with air temperature and pressure control (up to 10 bar)
High-reactivity fuel system	Common-rail 2.0 with twin-needle injector and multi-injection capability
Low-reactivity fuel system	Low-pressure, multipoint, and upstream of the intake valves
Valvetrain	Four valves with variable intake valve closure (VIC) and fixed exhaust valve opening (EVO)
Emission system	Horiba Mexa-One (NO_X, CO, THC, CO_2, and O_2) and AVL415S (FSN-soot)
Indicative system	AVL Indicom and a cylinder pressure transducer Kistler 6124A, with a 300-bar range and 30 pC/bar sensitivity
Engine control	Rapid prototyping platform
Test fuels	ISO 8217 compliant LFO/LNG (MN = 80)

AVL Indicom software (version 2015) and a Kistler 6124A cylinder pressure transducer with a 300-bar range and 30 pC/bar sensitivity were set up for measuring combustion-related specifications and storing them. AVL Indicom enables real-time data analysis from sensors. The Kistler 6124A transducer measures cylinder pressure with high precision. Its 300-bar capacity covers most engine pressures, and its 30 pC/bar sensitivity ensures detailed pressure change detection.

Changes were made to the injector piston alignment to accommodate RCCI-like early injections of the high-reactivity fuel (HRF). A centrally mounted twin-needle injector, enclosed within a high-pressure, common-rail fuel system, was optimized for the light fuel oil (LFO) used as HRF [38]. For RCCI injections, the smaller of the two nozzles was used to facilitate atomisation of the micro-injected quantities. With early injection timings, the narrow-cone injector tip supported proper reactivity stratification without extensive wall wetting. Natural gas, the low-reactivity fuel (LRF), was injected through a multipoint gas injector located upstream of the intake valve. The SCRE incorporates a partially variable intake/exhaust valvetrain.

Unlike a multicylinder engine, the SCRE did not feature a turbocharger, necessitating specific solutions to regulate charge air temperature and pressure. The complete charge air system comprises two compressors, two buffer tanks, a charge air dryer, and two pressure-regulating valves. This setup serves to control the charge air pressure and temperature while stabilising the airflow, thereby simulating the exhaust system of the actual production engine.

For the purpose of this research study, the detailed engine air path has been modelled in GT-Power software (version 2022) with the following assumptions. The intake and exhaust geometry are modelled in full detail, including the mentioned buffer tanks for exact flow calculations. Instead of modelling the complete gas regulating unit (GRU), a

simplified configuration with a single injector component was used to regulate the pressure in the gas supply system before delivering it to the engine through port fuel injection. Other than that, the model included a standard map-based direct injector for the HRF and a four-valve, rotational position-based valvetrain. Discrete variable valve actuation was imposed by predefined valve profiles. Figure 1 presents the governing model's subsystems. Note that the actual test setup did not involve the exhaust aftertreatment, which has been separately identified for the purpose of the present study. Section 3.3 provides the corresponding details of the aftertreatment model.

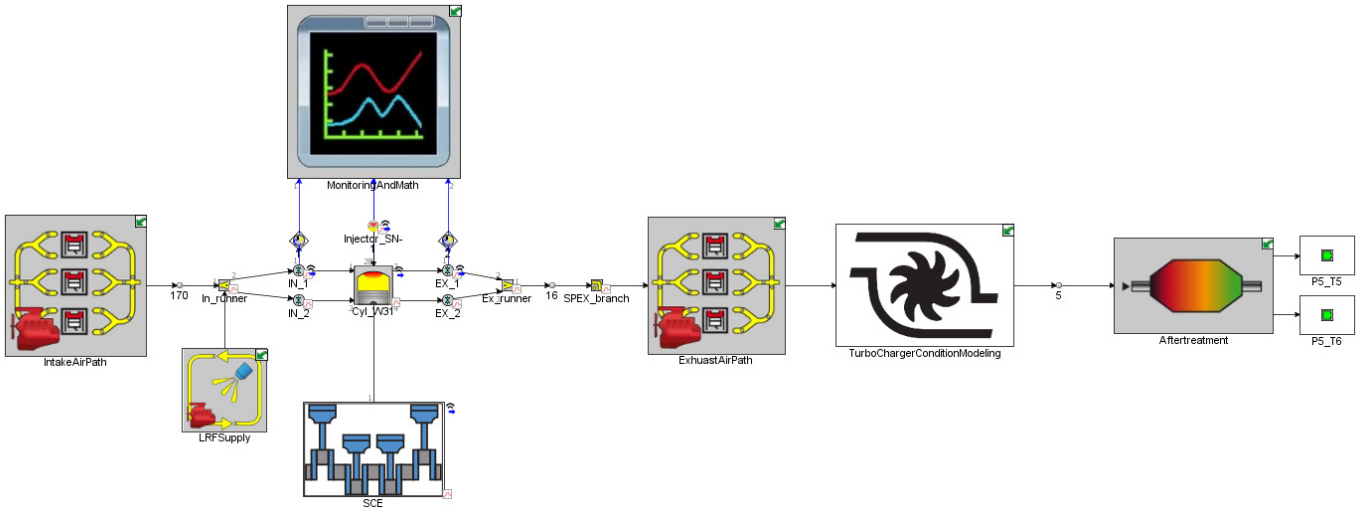

Figure 1. A 1D air-path model of the Wärtsilä SCRE layout in GT-Power.

In the GT-Power simulation, the modelling of turbocharger output conditions incorporated an orifice and an intercooler, as depicted in Figure 1, positioned between the muffler and the exhaust air path. The orifice's diameter has been optimised to ensure the desired pressure output. Additionally, the intercooler has been fine-tuned to maintain the turbocharger's temperature at the desired level.

The baseline air-path model (without aftertreatment) underwent thorough calibration against experimental data spanning 40 RCCI operating cases. Calibration involved conducting a three-pressure analysis (TPA) in GT-Power, as depicted in Figure 1. The measured in-cylinder pressure was matched to the simulated value by adjusting the flow and friction multipliers in the physical air-path model. More information on the TPA is available in the source document [39].

The calibration results have been thoroughly discussed in another paper by Kakoee et al. [34]. For transparency, they are synthetically reproduced in Figure 2, which illustrates a 0% error line (y = x) representing the simulated output on the *Y*-axis and the experimental output on the *X*-axis for four governing engine parameters. As the exact values of the data were confidential, only the ratio of simulated and experimental data has been shown as a cross-sign on the graphs. The calibration accuracy targets for the governing model parameters are depicted by dashed lines. The targets were stringent, representing the accuracy of steady-state measurement. Either device uncertainty or standard deviation, whichever was higher, was adopted as the measurement error.

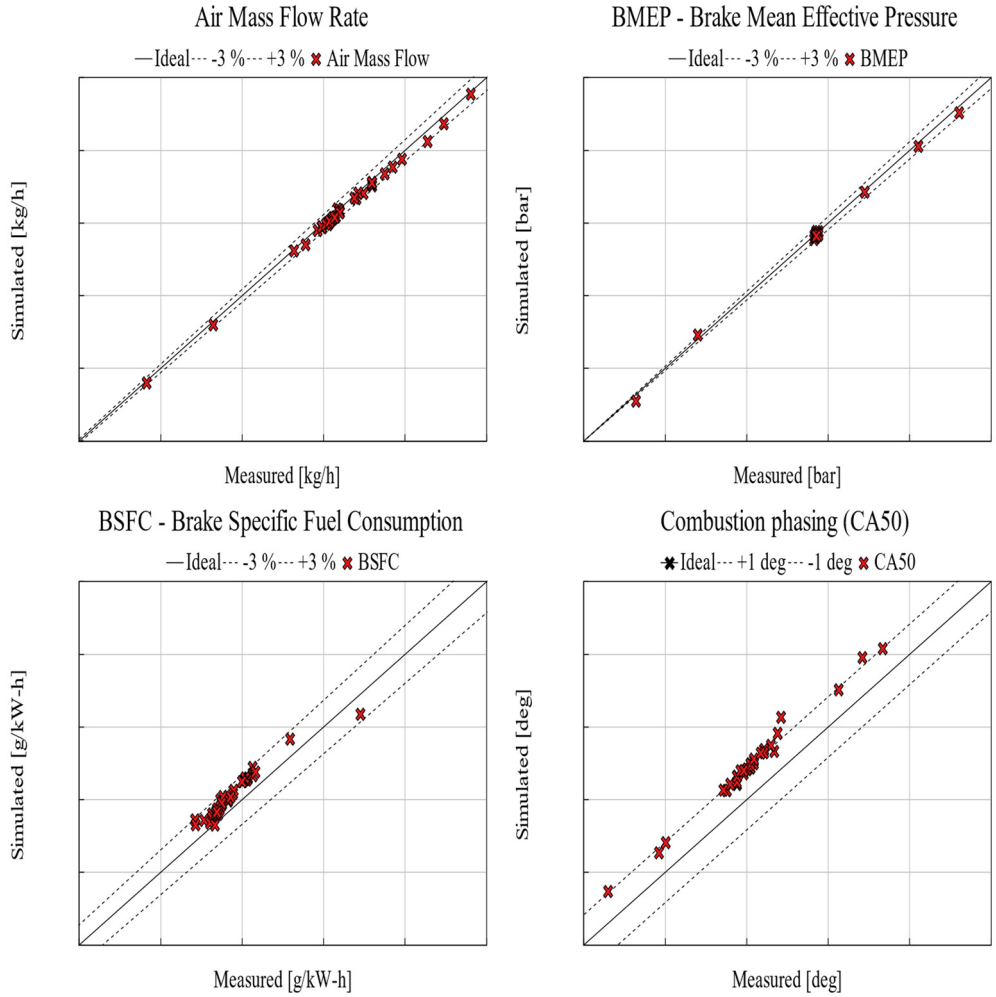

Figure 2. Baseline air-path model calibration results from three-pressure analysis in GT-Power.

Although calibrating the engine air-path model involved exploring various specifications, the four key parameters shown in Figure 2 were chosen to highlight the model's accuracy. Brake-specific fuel consumption stayed within a maximum error of 3 percentage across all 40 operating points, and the BMEP error remained under 3%, ensuring precision in each case. Divergence of the dashed lines in the figures indicates that in the higher value of specifications, deviation from the ideal line was higher. BSFC and CA50 in all operating points approximately had the same amounts of deviation in various loads, where higher BMEP and air mass flow rate show high deviations.

Examining the air-path dynamics, the air mass flow rate, a crucial indicator for flow accuracy, demonstrated deviations below or equal to 3%. Turning to combustion, the CA50 metric was selected to showcase simulation accuracy in predicting combustion phasing. CA50 exhibited an error of approximately 1.7 CAD, below the 2 CAD threshold and within the study's acceptable error range.

The UVATZ model, introduced by A.Vasudev et al. [35], simulates in-cylinder combustion. It was capable of simulating various low-temperature combustion concepts driven by chemical kinetics; it was parameterised in this study for natural gas and diesel-fuelled RCCI combustion. The UVATZ model considered the dominant factors influencing combustion, such as fuel and thermal stratification, in-cylinder turbulence, intake valve closure (IVC) temperature, and the composition and quantity of residual burnt gas. The combustor is divided into 12 zones, as depicted in Figure 3. The last two disc-shaped zones represent the cylinder head and piston boundary layers. The remaining 10 zones are annular, with zone

1 adjoining the liner. This zonal arrangement captures the bulk inhomogeneity resulting from compositional and thermal stratification, as shown schematically in Figure 3.

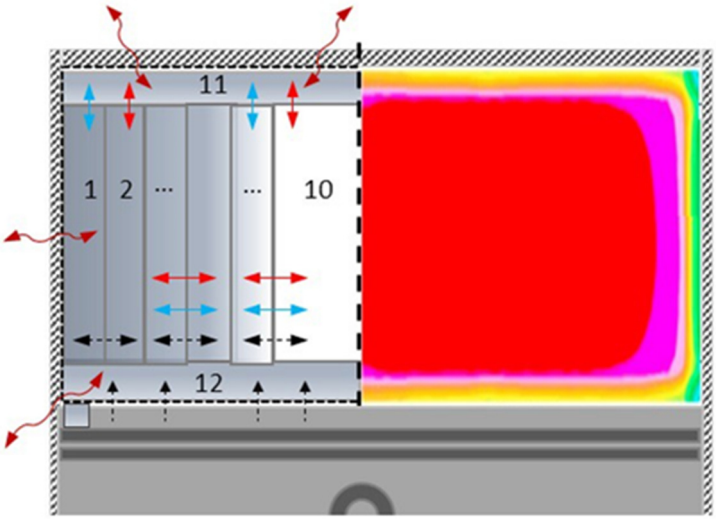

Figure 3. Conceptualisation view of the UVATZ multizone model (**left**) vs computational fluid dynamics representation of in-cylinder temperature stratification (**right**); red arrow—heat flow; blue arrow—mass flow; black arrow—work, number in the figure are zones index in simulation.

Interactions between the zones are modelled through heat, mass, and work transfer. Heat loss to the walls was accounted for using the correlation proposed by Chang et al. [40]. Transport of heat and mass between zones was modelled using gradient-based methods, while turbulence effects were incorporated following the approach of Yang and Martin [41]. The turbulence submodel involved a single calibration constant ζ_u. Chemical reactions were modelled using the mechanism developed by Yao et al. [42], which includes 54 species and 269 reactions. The HRF is represented by n-dodecane ($nC_{12}H_{26}$), while the LRF is defined as a mixture of CH_4 and ethane (C_2H_6).

The stratification of HRF was described by a simplified injection model, where the $nC_{12}H_{26}$ mass was assumed to be linearly distributed across the zones, with the liner zone having the highest concentration. This distribution was imposed at the moment of injection, and the enthalpy of evaporation was considered proportional to the mass of HRF in each zone. The specific profile gradient, ζ_∇, was adjusted to match the case-dependent requirements. The UVATZ model was implemented in C++ and used the thermochemical libraries of Cantera. The simulations were performed using the robust CVODES solver, with each closed-cycle simulation typically taking around three minutes to complete.

3.2. The Aftertreatment Model

As explained in the Section 2, this study focused on the coupling effects of engine gas exchange, RCCI combustion, and working conditions of the MOC, rather than the optimisation of catalytic efficiency. The primary catalyst materials and design used in diesel oxidation were chosen for current investigations. One should note that this catalyst chemistry has been thoroughly validated [37].

Figure 4 illustrates the catalytic brick. Its dimensions were carefully chosen for optimal performance, based on engine cylinder size, operating conditions, gas dynamics research data, and general requirements for the RCCI-tailored MOC [33,34]. A round-profile substrate brick with a diameter of 300 mm was used, which was close to the engine's exhaust geometry. The baseline brick length was set to 400 mm with 5 mm discretisation in the longitudinal direction for calculations. Catalyst cells were considered square, with a density of $2/cm^2$ and a wall thickness of 0.015 cm. These dimensions provided subsonic gas flow velocity and protected the system against backflows under all conditions. Variable cell densities and brick lengths were examined to study their effects on gas dynamics and catalytic

chemistry. The catalyst's substrate was covered with a 0.01 cm thick washcoat layer. The PGM physical properties have two adjustment factors: loading of the site element, i.e., the mass of the washcoat in the unit of volume, and atomic weight. These two specifications were 97 gr/ft^3 and 167.2 g/mol, respectively. The PGM in question was based on Khosravi et al.'s catalyst selection, which was a monolith commercial one and consists of platinum (Pt) and palladium (Pd) with 4:1 mass ratio [37].

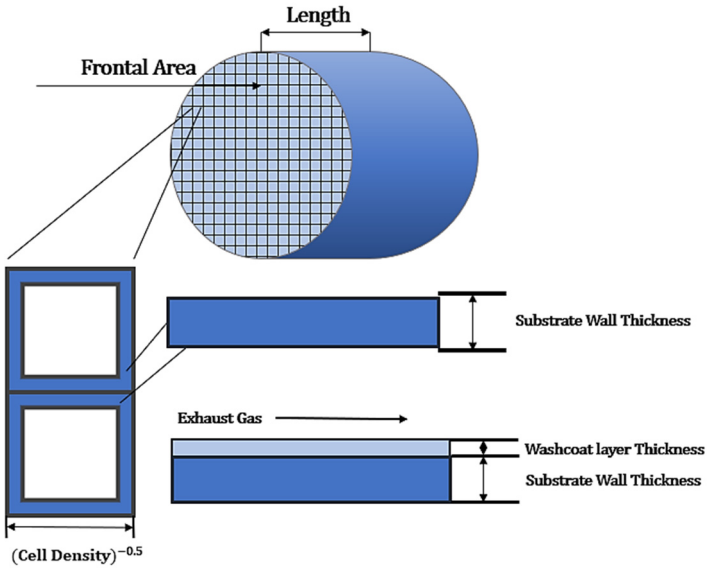

Figure 4. Catalyst brick specifications selected for MOC/DOC aftertreatment system.

The initial temperature of the catalyst brick's wall during the simulations was adjusted to 10% below the last part of the exhaust air path. The substrate material was cordierite, selected from GT-Power's library, with temperature-dependent specific heat, while the washcoat alumina specific heat was considered constant. This approach also was used in Khosravi et al. in an investigation of a DOC PGM catalyst [37].

The reaction mechanism used in this study was selected from the same work; however, it needed to be tailored to include specifics of the exhaust compositions of the RCCI engine. The implemented chemistry model is presented in Tables 2 and 3, and detailed considerations regarding its final formulation can be found in Appendix A.

Table 2. Hydrocarbons, hydrogen, and CO oxidation specifications in presence of PGM catalyst.

Catalyst	Reactants	Products	Pre-Exponential	Activation Energy	Concentration Expression
PGM	$CO + 0.5O_2$	CO_2	1.183×10^{12}	−81.33	$\{CO\} \times \{O_2\}/(G\ (1) \times G\ (2))$
PGM	$C_2H_6 + 3.5O_2$	$2CO_2 + 3H_2O$	1.266×10^{19}	−129.4	$\{C_2H_6\} \times \{O_2\}/(G\ (1) \times G\ (2))$
PGM	$H_2 + 0.5O_2$	H_2O	98,300	15.31	$\{H_2\} \times \{O_2\}/(G\ (1) \times G\ (2))$
PGM	$CH_4 + H_2O$	$CO + 3H_2$	1.20×10^{16}	106	$\{CH_4\} \times \{H_2O\} \times G\ (3)^2/G\ (2)$
PGM	$CH_4 + 2O_2$	$CO_2 + 2H_2O$	9.00×10^{16}	−80	$\{CH_4\} \times \{O_2\} \times G\ (3)^2/G\ (1)$
PGM	$C_2H_6 + 2H_2O$	$2CO + 5H_2$	7.00×10^{17}	118	$\{C_2H_6\} \times \{H_2O\} \times G\ (3)^5/G\ (2)$
PGM	$CO + H_2O$	$CO_2 + H_2$	5.60×10^{17}	67.5	$(\{CO\} \times \{H_2O\} - \{H_2\} \times \{CO_2\}/G\ (4)) \times G\ (3)^2/G\ (2)$
PGM	$C_2H_4 + 3O_2$	$2CO_2 + 2H_2O$	1.01×10^{19}	−119.4	$\{C_2H_4\} \times \{O_2\}/(G\ (1) \times G\ (2))$
PGM	$C_2H_4 + 2H_2O$	$2CO + 4H_2$	7.50×10^{17}	108	$\{C_2H_4\} \times \{H_2O\} \times G\ (3)^4/G\ (2)$

Table 3. General and inhibition function in system of modelled reaction.

G Functions	Description	General and Inhibition Function
G (1)	CO and CO_2 inhibition	$(1.0 + 248.0 \times \exp(-614.9/T) \times \{CO\})^2$
G (2)	hydrocarbon inhibition	$(1.0 + 2.02 \times 10^{-17} \times \exp(2.82 \times 10^4/T) \times (\{DF\} + \{DF\}))^2$
G (3)	conversion factor	$(8.314 \times T)/P$
G (4)	water–gas shift equilibrium constant	$\exp(-1 \times (-41034 + 44.19 \times T - 0.005553 \times T^2)/8.314/T)$

3.3. Model Coupling Assumptions

The UVATZ model has been coupled with a 1D air-path model in GT-Power for predictive simulations of the RCCI engine. The coupling was achieved by using GT-Power's external cylinder object. The UVATZ model was integrated into a dynamically linked executable, enabling the division of responsibilities between the two models. The air-path dynamics and gas exchange phase of the four-stroke cycle were handled by GT-Power, while the closed part of the cycle, specifically the combustion phase, was handled by the UVATZ model. Figure 5 illustrates the exchange of information between the two models. At intake valve closure (IVC), the UVATZ model received an input file detailing the mixture's thermodynamic state, geometric parameters, and solver settings.

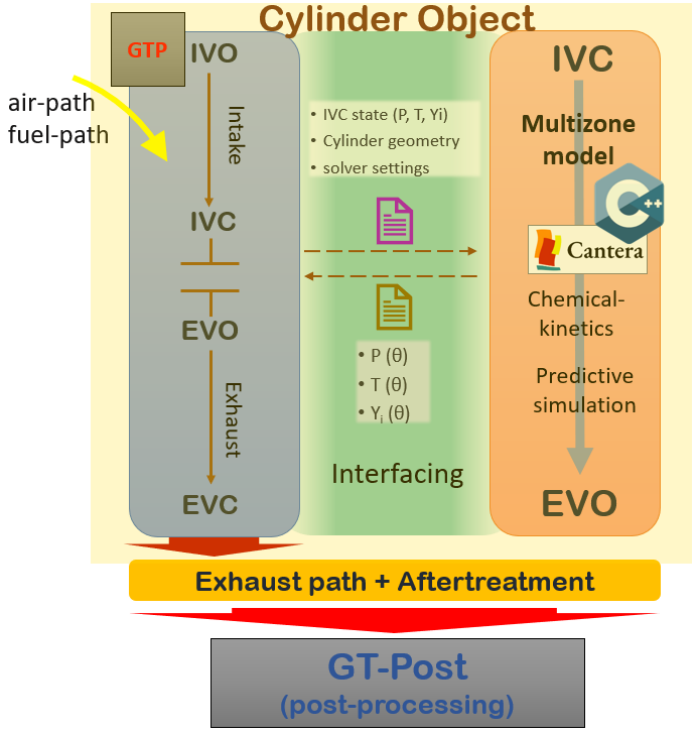

Figure 5. Schematic of data exchange between GT-Power and UVATZ model in coupling methodology.

It is important to highlight that the predictive cylinder's wall temperature has been used, providing boundary conditions for the UVATZ heat loss model (Woshini-Chang [40]). Specifically, the UVATZ model's heat loss calculations used surface temperatures of the cylinder head, piston, and liner. Following the combustion phase, the simulation results, such as the cylinder-averaged histories of the thermodynamic state and species concentration (from the chemical kinetic mechanism), were transferred back to GT-Power through an output file.

This coupling procedure allowed for streamlined postprocessing within GT-Post (GT-Suite's postprocessing tool), simplifying the analysis of the results from both the combustion and aftertreatment models. An "aftertreatment inlet" subassembly was created to pass the output species concentration to the catalyst brick. The cycle-averaged mass flow, temperature, and species concentrations were transferred from the explicit circuit to the quasi-steady (QS) circuit, the recommended flow circuit for the aftertreatment chemistry solver. The transferred species included CO_2, CO, H_2O, CH_4, C_2H_6, C_2H_4, N_2, O_2, H_2, and $nC_{12}H_{26}$, which were supposed to be collected in the QS inlet circuit. The temperature in the QS circuit came as direct result of the physical simulation taking into account the heat losses in the exhaust components. The exhaust wall temperature was calculated dynamically within the cylinder.

One should note that exhaust backpressure in the SCRE was regulated with a back-pressure valve to mimic the conditions of the production engine with a turbocharger. Accordingly, an adjustable orifice was added before the aftertreatment block. Furthermore, a charge air cooler with controllable efficiency mimics the temperature drop behind the turbocharger. Both objects are within the "turbocharger conditioning" block visible in Figure 1. The parameters were tuned case-dependently to represent the pressure/temperature drop in a production version of the Wärtsilä 31 engine. The end environment conditions were set to ambient to prevent backflow through the catalyst.

3.4. The Scope of the Research

The coupled system-level model has been used to perform simulations to determine the feasibility of the RCCI—MOC marine engine. Figure 6 summarises the creation of this GT-UVATZ aftertreatment modelling framework. The entries in blue are the enabling methods and those in green are the resultant simulations presented in the Section 4.

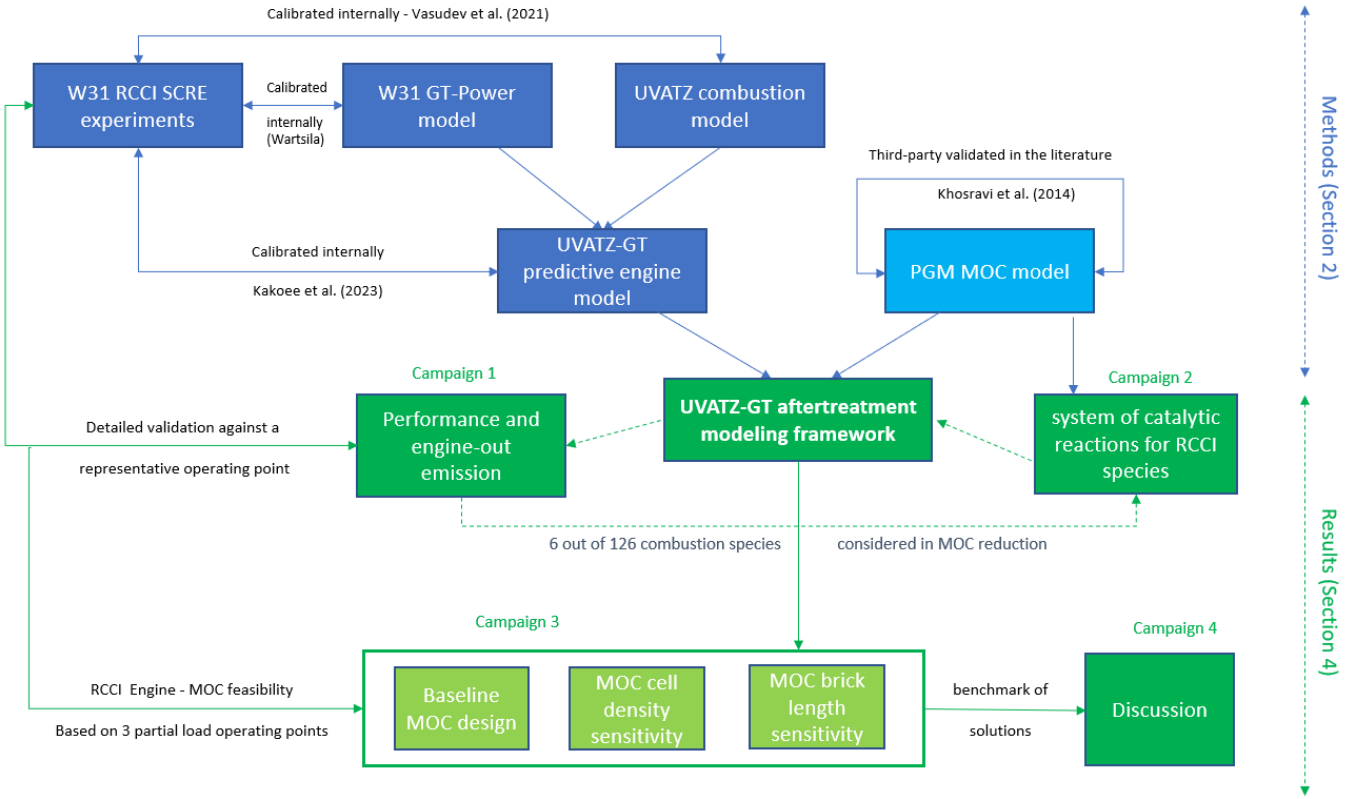

Figure 6. Workflow and scope of research [21,22,29].

The simulation plan for this study involved three dedicated campaigns (Figure 6). Campaigns 1 and 2 secure that independently validated submodels incorporating the frame-

work were valid for the present study. To this end, campaign 1 evaluated the performance and thermal state of the coupled engine model and validated the simulation result against the corresponding experimental data from the Wärtsilä RCCI test campaign (refer to the Section 3). Analysis of the simulated exhaust components allowed for the formulation of a proper system of reactions to be embedded into the MOC model. This was carried out in campaign 2 resulted from fundamental considerations supported by preliminary simulations. The completed engine aftertreatment model with proper chemistry was used in campaign 3, where the final solution was assessed involving geometric optimisation of the aftertreatment block. This entailed model-based sensitivity analysis on MOC cell density and brick length.

Three experimental operating points were selected as the baseline for the simulations. All of them represent partial-load RCCI operation, where methane slip has been considered problematic. Table 4 provides relevant data characterising these operating points. Note that all points have ultra-early diesel start of injection (SOI), characteristic of RCCI. Injection commences close to IVC to assure proper premixing of natural gas and diesel. All test point data in Table 1 were relativised against reference values (ref) for confidentiality reasons. The reference values correspond to the standard IMO (International Maritime Organization) Tier III low-load calibration points for the commercial version of the Wärtsilä W31DF, a multicylinder, lean-burn, NG–diesel engine.

Table 4. Selected operating points from SCRE test campaign used as baseline for study.

Case	Scope	Load [%]	λ [–]	BR [pp]	SOI [°CA bTDC]	T_{int} [K]	P_{int} [bar]
A	Investigation	11	ref + 1.8	ref − 41.9	ref + 65	ref	ref + 0.5
B	Validation and investigation	25	ref + 1.0	ref − 10.9	ref + 65	ref	ref + 1.3
C	Investigation	50	ref + 0.8	ref + 2.4	ref + 65	ref − 5	ref + 3.5

Testing aftertreatment performance across a variety of RCCI operating conditions entailed significantly different calibrations for each of the three test points. SOI remained fixed, but intake charge pressure (Pint), temperature (Tint), and air–fuel ratio (λ) were all varied. Note that the natural gas/diesel blend ratio (BR) definition used here was based on energy content.

4. Results and Discussion

4.1. Validation of the Engine Aftertreatment with the Predictive RCCI Combustion Model

The predictive RCCI combustion model has been thoroughly calibrated in earlier studies [4,35]. The latest version of the UVATZ model dynamically coupled with GT-Power was thoroughly investigated in Kakoee et al. [34], proving predictive capabilities with errors below 4% for key combustion parameters. Due to the model's predictive nature, the engine air path and combustion object did not require recalibration for the present study. The addition of the aftertreatment had little impact on the upstream conditions, so only one case outside of the calibration space (Case B, Table 2) has been chosen to discuss the model's validity in terms of parameters relevant to this aftertreatment coupling study.

4.2. Performance Results and Exhaust Thermal State

The UVATZ model coupled with the GT-Power engine model can predict the heat release rate and resulting in-cylinder pressure using only basic inputs, as set out in Table 3. All of the other combustion indicators can be derived from those two fundamental quantities. Figure 7 shows the simulated results for Case B against the corresponding experimental results (in-cylinder pressure) postprocessed with TPA (HRR). The model's high accuracy and its phenomenological correctness is evident from Figure 7. The root mean square (RMS) error in pressure was below 1 bar and the corresponding deviation in HRR is 37J. Both

errors were within the cycle-to-cycle variations in the experimental results. Note that the model is able to reflect the phenomenology of the process, with distinguishable negative temperature coefficient (NTC) reactions (preignition), followed by the autoignition of fuel-rich zones (the first peak in HRR) and the reactivity stratification-controlled combustion of the bulk of the in-cylinder mixture (the main HRR peak).

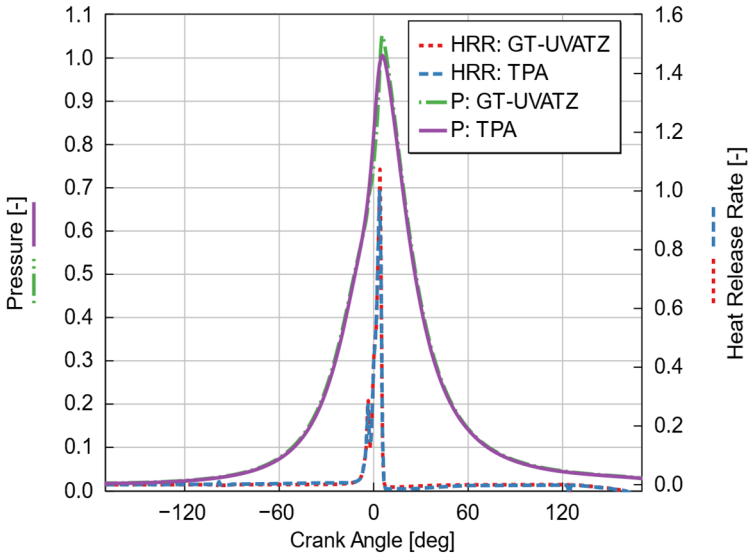

Figure 7. Normalised pressure and heat release rate simulated with GT-UVATZ model, with results from three-pressure analysis (TPA) applied to experimental data for Case B.

These features are better captured in Figure 8b, which shows the cumulative heat release (CHR) around the combustion event. The experimental and simulated CHR traces in Figure 8b coincide within the error of experimental procedure. The experimental CHR's (TPA air-path model [34]) increased before combustion and its decline after combustion was unrealistic and came from the fact that the mixture's composition during combustion, characterised by the ratio of specific heats (γ), cannot be acurately determined experimentally. Instantaneous gamma in the model is calculated explictly from kinetic-driven detailed composition, so the simulated CHR exibits the correct trends.

Figure 8a depicts the corresponding differences in specific heat ratio. The close match of simulated values to those extrapolated from the experimental data (RMS = 0.0271) confirmed that the mixture composition was well reproduced by the model. As mentioned, combustion indicators like a crank angle of 10% and 50% mass of fuel burned (CA10 and CA50, respectively) can be further derived from the CHR. CA10 was observed at -4 CAD aTDC (after top dead centre) for the coupled model, and at -5.5 CAD aTDC for the experimental case. CA50 was at 2.5 CAD aTDC for both the simulation and experiment. The accuracy of these simulation results has been considered more than sufficient for the purpose of the present study, considering that cycle-to-cycle variations in experimental CA10 were of the order of ± 1 CAD.

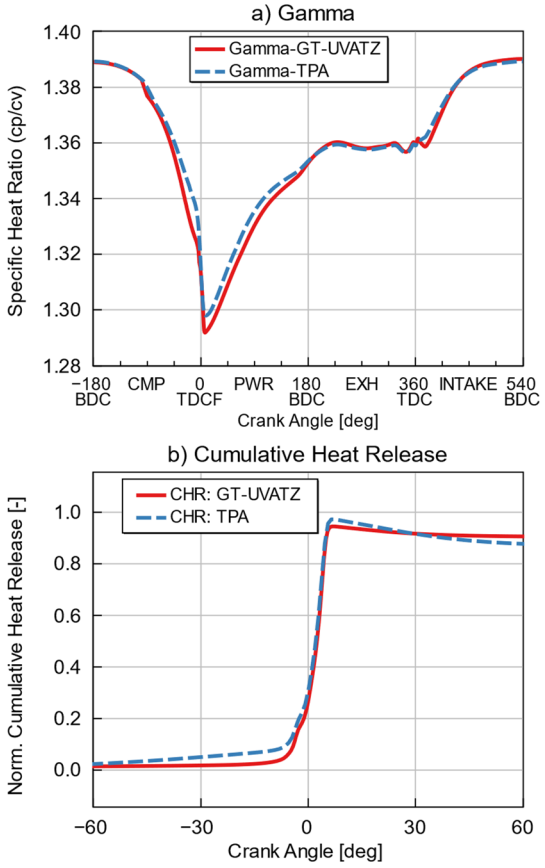

Figure 8. Specific heat ratio (γ) (**a**) and cumulative heat release rate (**b**) for TPA and GT-UVATZ models: Case B.

Figure 9 shows how the discussed uncertainties in combustion estimation transfer to general engine performance factors and thermodynamic variables relevant for aftertreatment performance. The accuracy in reproducing the instantaneous mixture composition comes from the combined accuracy of the air-path model and the combustion model, which co-determine exhaust composition. This can be demonstrated synthetically by volumetric efficiency (VE) and in-cylinder lambda (λ), which were reproduced by the model with an error below 1%. The resulting error in the net heat release rate (NHR) was within a similar range. The largest errors from all synthetic estimators were for maximum pressure (P_{max}) and indicated mean effective pressure (IMEP). Nevertheless, their accuracies were only slightly above the 1% threshold; typical experimental tolerances in these values are set between 2% and 4%.

The thermal stability of the GT-UVATZ model is an important consideration for aftertreatment studies. To this end, two main factors, namely, exhaust temperature and the mass flow rate at the exhaust runner, were considered and compared with the TPA results. Figure 10 illustrates the normalised mass flow rate (a) and the exhaust temperature (b). It is evident that the mass flow rate for the GT-UVATZ model and TPA results align closely in the exhaust branch, with an RMS error of 0.0737 kg/s, with less than 4% error in all points. The exhaust temperature error (Figure 10b) is higher, but the point-to-point percentage error is less than 5%, and the RMS error for the exhaust temperature is 23 K. It should be noted that exact exhaust temperature is usually hard to determine experimentally because the flow is unsteady and sensor readings are influenced by the pipe wall heat transfer. The average exhaust gas temperature measured experimentally in Case B was actually closer to the UVATZ-simulated results than to the TPA results. All of the above findings indicate that the GT-UVATZ model exhibits good thermal stability, with tolerable discrepancies in exhaust temperature.

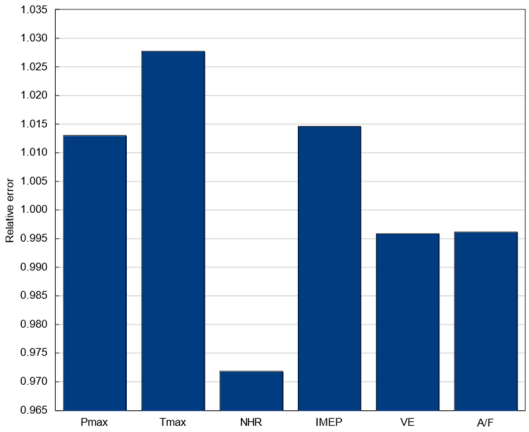

Figure 9. Engine specifications' error percentage of GT-UVATZ model in comparison with TPA: Case B.

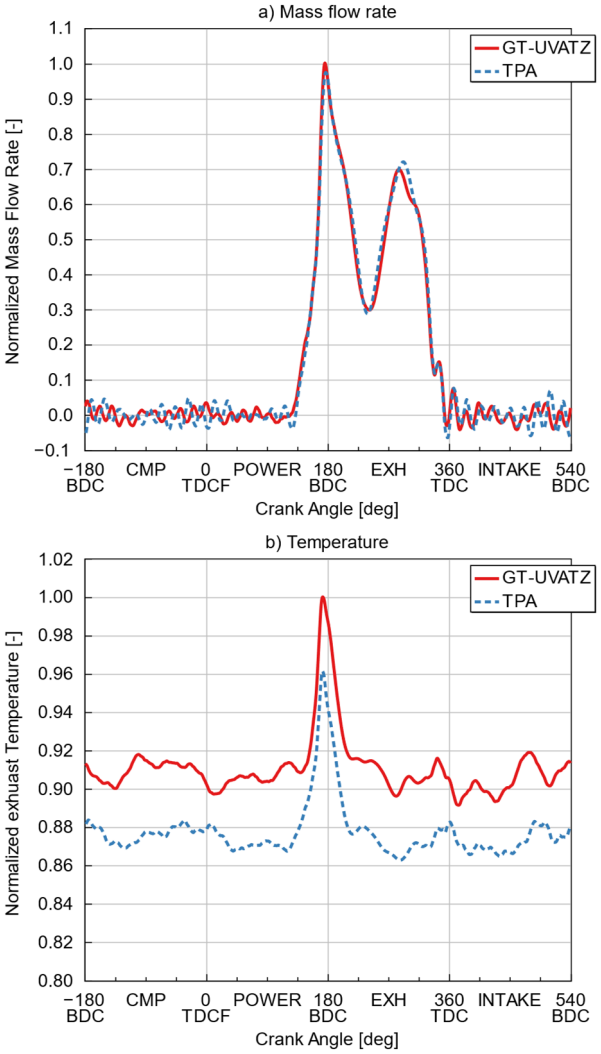

Figure 10. (**a**) Normalised mass flow rate and (**b**) temperature at exhaust branch for both GT-UVATZ and TPA air-path models: Case B.

4.3. Engine-Out Exhaust Composition

The design of the aftertreatment chemistry submodel required a detailed analysis of exhaust gas composition. In the adopted modelling approach, composition was determined by the combustion kinetic mechanism employed and by the operating point conditions

(lambda, blend ratio, etc.). Figure 11 provided the predicted exhaust composition in a control volume before the entering the catalyst block in case B operation point mentioned in Table 4. The simulation was run in ambient conditions in the exhaust towards converged results to provide a greater insight into the model's validity. Combustion was ultra-lean, so there was an abundance of oxygen present in the exhaust. Nitrogen and oxygen are excluded from Figure 11 for scalability reasons, likewise for other species with a converged molar fraction lower than 0.005%.

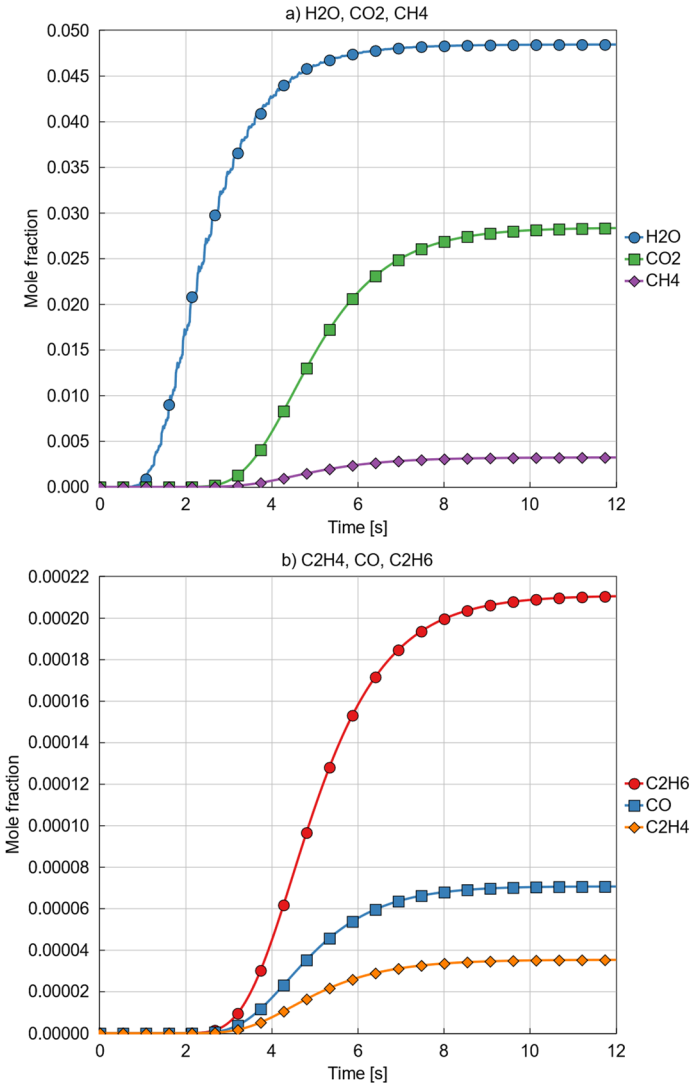

Figure 11. Concentrations of most important species in exhaust gas for Case B: (**a**) H_2O, CO_2, and CH_4; (**b**) C_2H_6, CO, and C_2H_4.

It is apparent from Figure 11 that the main exhaust components reached saturation after around 12 s of simulation and the model in the mid-load condition converged at 6 s (18 engine cycles). Apart from nitrogen and oxygen, H_2O was the main compound present in the exhaust in converged conditions, and its amount was roughly 1.8 times higher than CO_2. Around 15% (energy-based) of diesel was used to support autoignition at this operating point; therefore, slightly more CO_2 was created compared to pure methane combustion stoichiometry (2:1). As expected from RCCI, the main toxic exhaust components came from incomplete combustion and pertain to CO and unburned CH_4. Note that the difference between CO and CH_4 observed as the simulation proceeded was the result of the combustion model converging. RCCI combustion is very sensitive to IVC conditions, including the amount and composition of residuals. Therefore, the residuals trapped in the

cylinder caused a feedback loop between exhaust composition and the ensuing combustion. The model covered this phenomenon, which was better seen in the scale of intermediate hydrocarbon formation (C_2H_4). Both C_2H_4 and C_2H_6 (Figure 11b) influenced the combustion convergence, even though their concentrations were an order of magnitude smaller than that of CH_4. Both species were primarily a result of breaking the methane oxidation pathway. The amount of C_2H_4 was lower than C_2H_6 as the latter was also present in small amounts (below 1% on a mass basis) in the simulated natural gas. Apart from the discussed species, the SK54 combustion mechanism predicted distinguishing amounts of aldehydes and formic acid as the most prominent groups. Their cumulative concentration in the exhaust at the discussed operating point was comparable to that of N_2O. All of those species can have a poisoning effect on catalyst performance [43,44]. However, as the experimental results cannot verify their amounts in simulated engine-out and aftertreatment engine-out flows, they will not be further included in the design of MOC chemistry for this initial feasibility study. Poisoning effects will be the topic of a separate publication.

Figure 12 provides a data reference for Figure 11's results, comparing the simulated saturated values with the available measurement data from the corresponding case realised on the test bench.

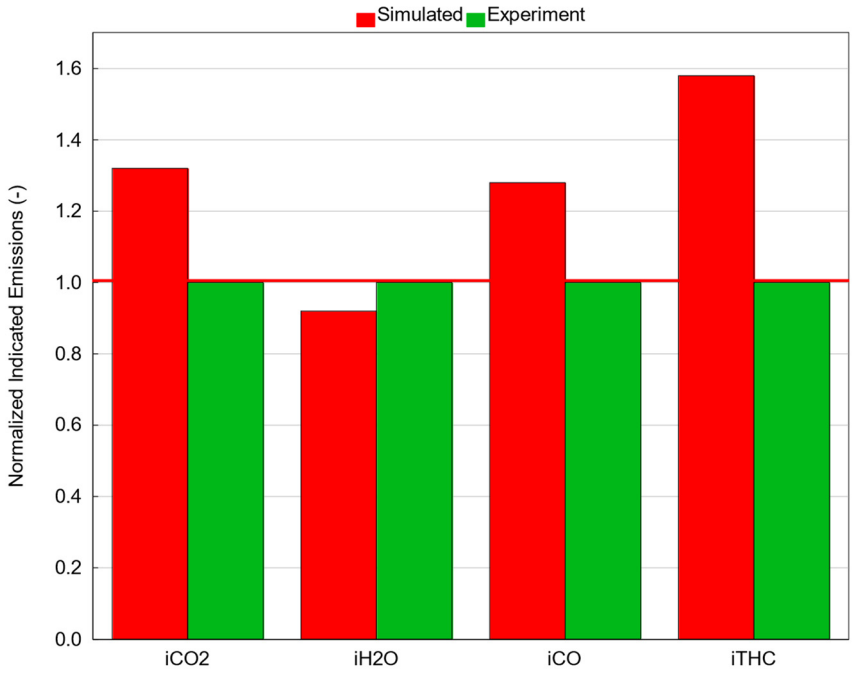

Figure 12. Comparison of experimental and simulated results of some important exhaust emissions.

It is shown that the results were of the same order of magnitude, and that the overestimation in simulated CO and THC data was compensated for by the corresponding difference in CO_2. One should note that the model was calibrated on a different engine, and emissions were not explicitly tuned in this campaign. In that respect, the size of the boundary layer heavily influenced the unburned hydrocarbon results in the UVATZ model. The boundary layer size is hard-coded here and was not subjected to tuning, which might explain the overestimation of THC. Finally, one should note that explicit accuracy in emissions was not a target for this category of models, as they do not capture the detailed geometrical effects of the combustion chamber. Nevertheless, the model was fully predictive and captured proper trends for emission formation between different engine sizes and different operating points in the RCCI regime. The above discussion substantiates the feasibility of the obtained emission results from the perspective of the combustion concept and the aftertreatment design.

4.4. Functional Validation of the Aftertreatment Model

This section gives a detailed analysis of partial results obtained from the aftertreatment system, employing the adopted chemistry model. Case B was the primary focus, serving as a validation benchmark for the engine-out model results discussed in Section 4.1. Figure 13 presents contour depictions of the complete engine air path, providing a comprehensive functional validation of the thermal state for the converged simulation. The exhaust registered the highest temperatures, exceeding 650 K, after the cylinder, with a minor drop along the exhaust path caused by heat loss. A significant shift in temperature was evident after the turbocharger conditioning section, where it decreased from 670 K to 552 K. This notable drop underscores the significant influence of the intercooler in achieving realistic exhaust temperature conditions. The backpressure caused by the turbocharger block was also evident. The system outlet temperature and pressure were determined by the preset ambient conditions.

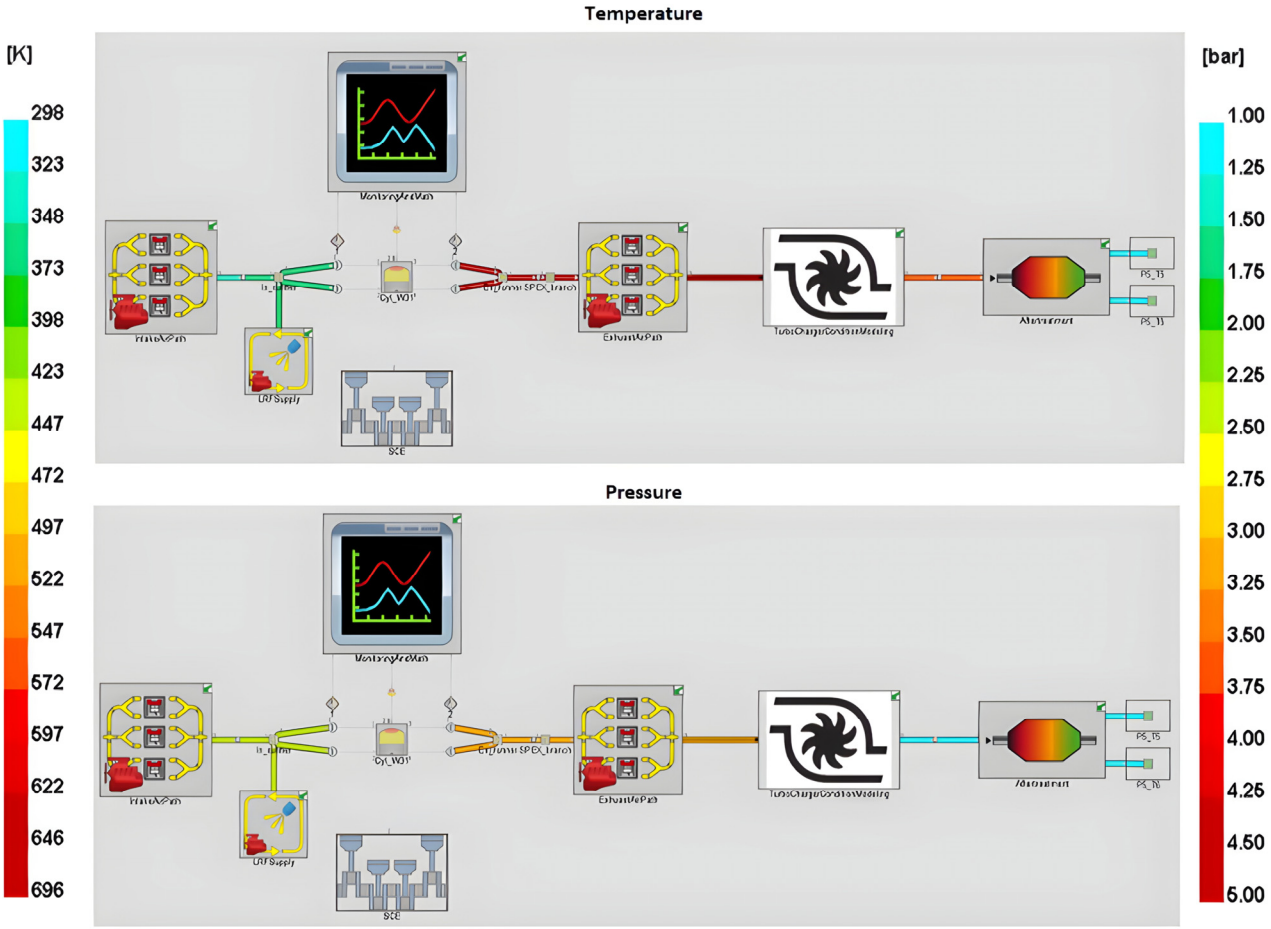

Figure 13. Temperature and pressure contour of air-path model for Case B.

Temperature management within the aftertreatment block is important for its effective operation. Figure 14 depicts the inlet temperature of the catalyst brick during steady-state engine operation, with the outlet temperature gradually increasing to converge with the inlet temperature. Notably, the temperature at the inlet is within the functional range for the MOC, i.e., above the light-off threshold yet below the 640 K boundary of thermal durability [33].

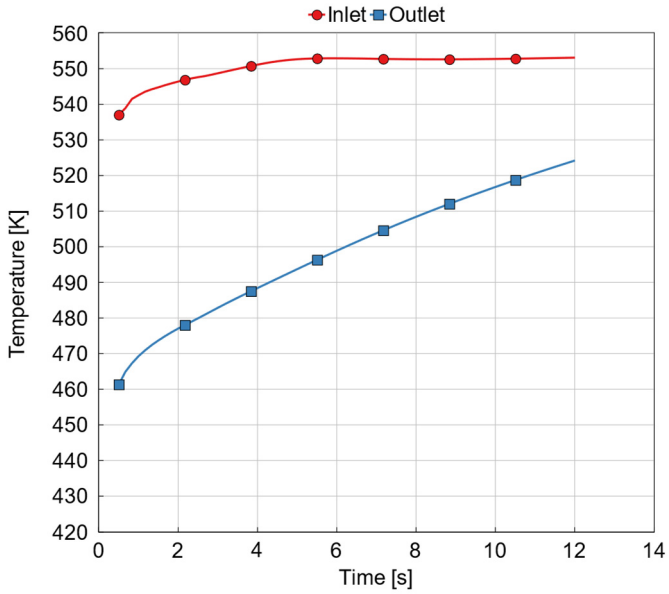

Figure 14. Mass-averaged temperature at inlet and outlet of catalyst brick: mid-load case; L = 400 mm and cell density = 2 (1/cm^2).

It can be concluded that as the simulation progressed over a longer timeframe, it is apparent that the inlet/outlet temperature eventually became saturated due to exhaust and catalyst walls reaching converged temperatures. The inflection in the temperature timeseries, observed within the initial 3 s of simulation, was the result of the combustion convergence. The cylinder was initiated with elevated cylinder wall temperature through the first few cycles. This was to avoid sustainable misfire, as RCCI combustion is very sensitive to in-cylinder temperature stratification. While the cylinder thermal solver recalculated the wall temperature to a realistic level, the combustion efficiency reduced, which was evident from the engine-out emissions in discussed in Section 4.1. These saturate after approximately 4 s of simulation, causing the catalyst inlet/outlet temperature gradient to stabilise its slope, affected only by the exhaust pipe preheating.

Figure 15 illustrates the mole fraction of species considered in the catalytic reaction before and after the catalyst brick. It is evident that the conversion efficiencies of individual hydrocarbons are different. In the given operating conditions, the conversion efficiency of CH_4 was roughly 57.5%, (Figure 15a), while C_2H_4 and C_2H_6 converted at a 43.8% and 45.6% rate, respectively, (Figure 15b,c). The simulation converged with a cumulative THC conversion efficiency of 56.4%.

The results of intermediate hydrocarbon conversion in Figure 15 do not correlate directly to the activation energies of the catalytic reactions in Table 4, as they are the superposition of other factors. Species concentration plays an important role. The oxidation reaction of C_2H_4 had a significantly lower activation energy and pre-exponent coefficient but its precatalytic concentration was roughly half that of C_2H_6, which explains the similar conversion efficiencies. It should also be noted that although the conversion of C_2H_6 and C_2H_4 to other products was easier than CH_4 conversion, these results show that CH_4 conversion was greater than that of the other two hydrocarbons. The reason for this phenomenon is related to species concentration, where CH_4 needs more activation energy than the other two hydrocarbons. Interestingly, C_2H_4 has a similar activation energy as CO, but in both reactions for CO in Table 2, CO has a 10^4 lower order in the pre-exponential factor and is completely and almost immediately converted to CO_2. The adopted catalyst model yields results that are trend-wise comparable with the available literature, such as the results of Khosravi et al., which show approximately 100% of CO conversion in all test cases in the presence of various PGM types [37]. In a natural gas engine investigated by Mortensen et. al, it was observed in early engine operation that the conversion efficiency

of wet methane (the same condition as in the current study) started at 70% and gradually decreased [16]. The same methane conversion trend also occurred in the current study, as depicted in Figure 15. A similar trend was identified in a marine industry application, where methane conversion in a PGM catalyst aftertreatment system varied from 70% to 50% in early methane engine operation [30].

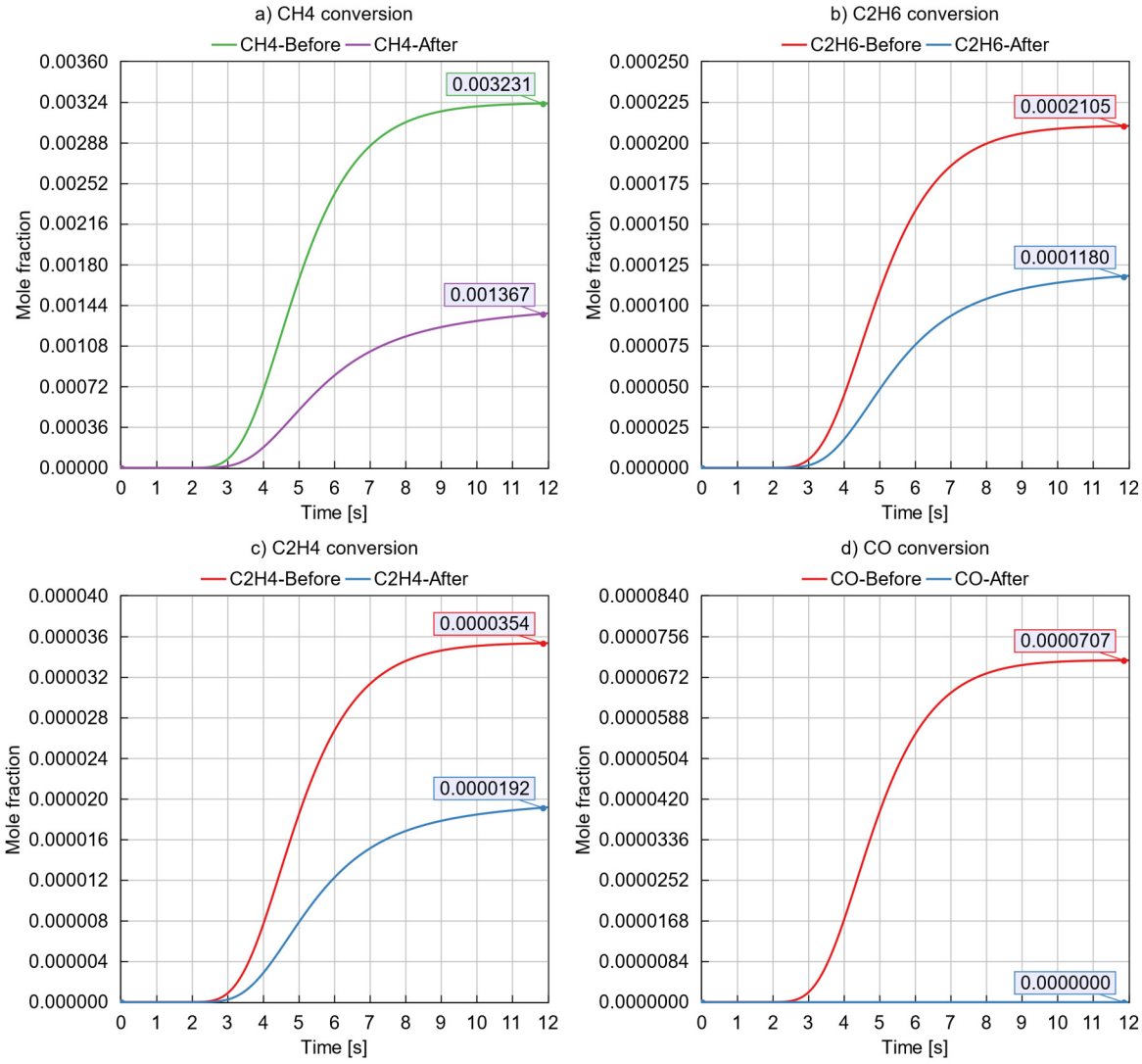

Figure 15. THC and CO mole fraction after and before catalyst brick: mid-load case; L = 400 mm and cell density = 2 (1/cm^2).

One can conclude from the above discussion that the engine–catalyst model coupling can be considered functionally valid. However, modelling aftertreatment simulation in GT-Power has certain limitations. Simplifications in chemical kinetics may lead to inaccuracies in predicting catalyst reactions. Spatial and temporal resolutions may not capture intricate details, affecting accuracy during rapid transients. Catalyst aging and poisoning effects might not be fully represented, and interactions with engine control systems may not account for dynamic coupling. Variability in the fuel composition and the challenge of experimental validation, especially under transient conditions, add complexity. Recognising these limitations is crucial for the accurate interpretation of simulation results and for refining models for more robust predictions in real-world scenarios.

4.5. MOC Performance at Representative RCCI Operating Points

The functionally validated model discussed above was further used to research the aftertreatment performance in all three investigated RCCI operating points listed in Table 3. The research focus was on conversion efficiency, light-off temperature, and the effect on overall engine performance.

4.6. Results with Baseline MOC Geometry

Figure 16a,b show the catalyst outlet mass flow rate and inlet temperature. Both were instrumental in examining the thermal stability and potential backflow conditions. Notably, the temperature at the catalyst inlet ultimately reached a stable point. While minor fluctuations were observed in the temperature, the mean temperature remained stable throughout the integrated engine and aftertreatment system. Additionally, the convergence temperatures for all three case studies aligned with the desired inlet temperatures, mirroring functionally accurate results. The mass flow rate also exhibited a degree of stability at the catalyst brick outlet, surpassing the stability observed in temperature conditions.

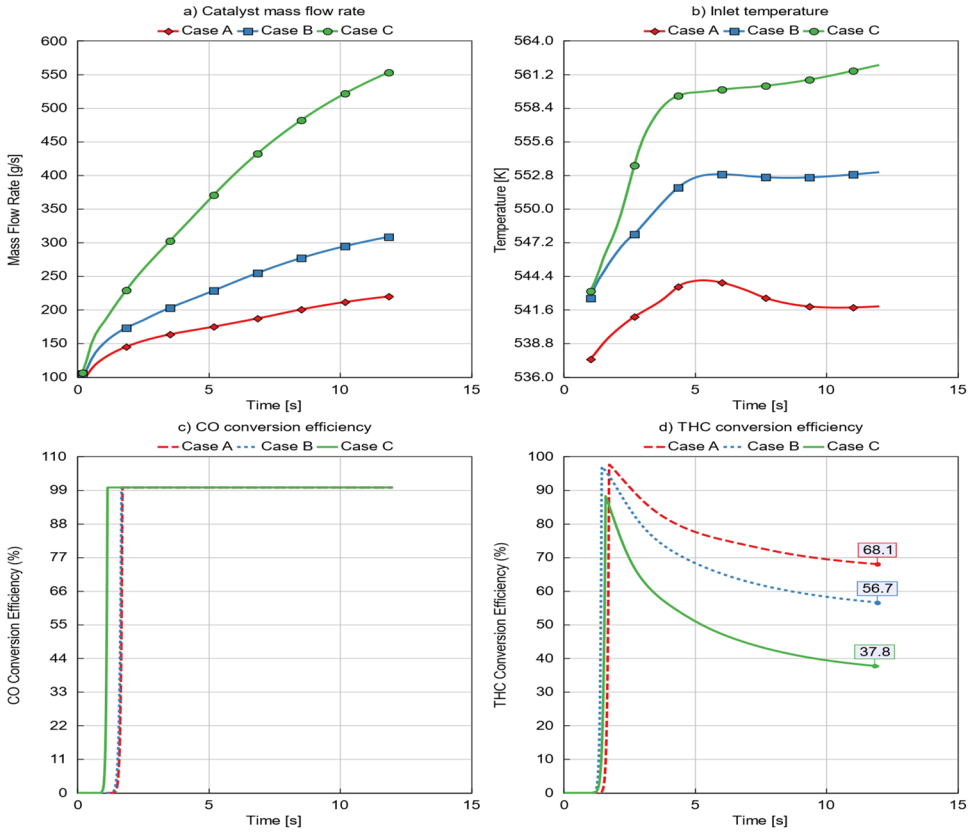

Figure 16. (**a**) Outlet mass flow rate, (**b**) inlet temperature, (**c**) CO conversion, and (**d**) THC conversion efficiency across three distinct case studies with L = 400 mm and cell density = 2 (1/cm^2).

Figures 16c and 17d illustrate CO and THC conversion efficiency. In all cases, as illustrated, CO was entirely converted into other species, predominantly CO_2. Notably, the low-load case achieved 100% conversion, albeit slightly higher than the other cases, highlighting a direct correlation between CO conversion efficiency and its concentration in the exhaust, as well as catalyst temperature. In contrast, the conversion of THC exhibited a non-monotonic trend. The conversion efficiency stabilised after some time, reaching 68.1% for the low-load case and 56.8% and 37.8% for the mid- and high-load cases, respectively. It is noteworthy that these conversion efficiencies were attained using a coarse catalyst mesh with a 2 (1/cm^2) cell density and a length of 400 mm. This difference in THC conversion can be related to higher average total hydrocarbon produced at higher loads.

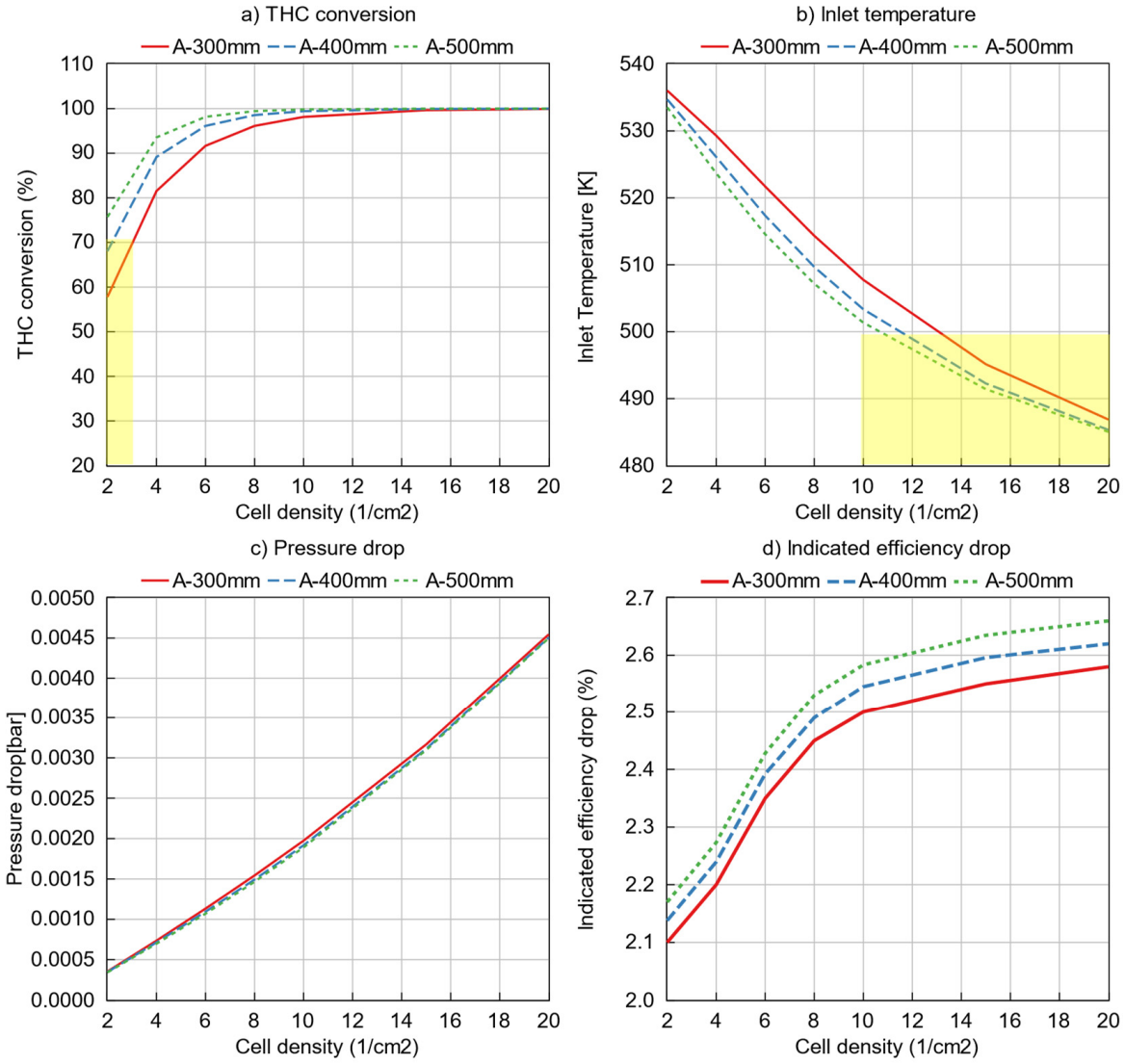

Figure 17. (**a**) THC conversion; (**b**) catalyst inlet temperature; (**c**) pressure drop across the engine; (**d**) gross indicated efficiency drop for low-load case (Case A) in various geometries and cell densities, yellow area illustrated un-desired domain.

The geometric configuration of the catalyst played a pivotal role in assessing the functional viability of the exhaust aftertreatment. Striking the right balance between mesh size and length was crucial, as overly fine meshes or excessive length can lead to undesirable pressure drops along the catalyst brick. Conversely, overly coarse meshes can compromise conversion efficiency. To address this, Figure 18 compares the pressure drop across all three load conditions. The pressure drop remained consistently below 10 mbar for all three cases [45,46]. Higher pressure drops, averaging around 6 mbar, were noted for the high-load scenario, while drops of only 1.2 mbar were observed for the low-load case. The mid-load case displayed an intermediate pressure drop of approximately 2.5 mbar.

Given the stable condition of the inlet temperature and the low pressure drop observed in the baseline model, it can be inferred that the integration of the aftertreatment system in this simulation study is feasible. Building upon this feasibility, the subsequent discussion delves into the geometric sensitivity of the installed catalyst brick.

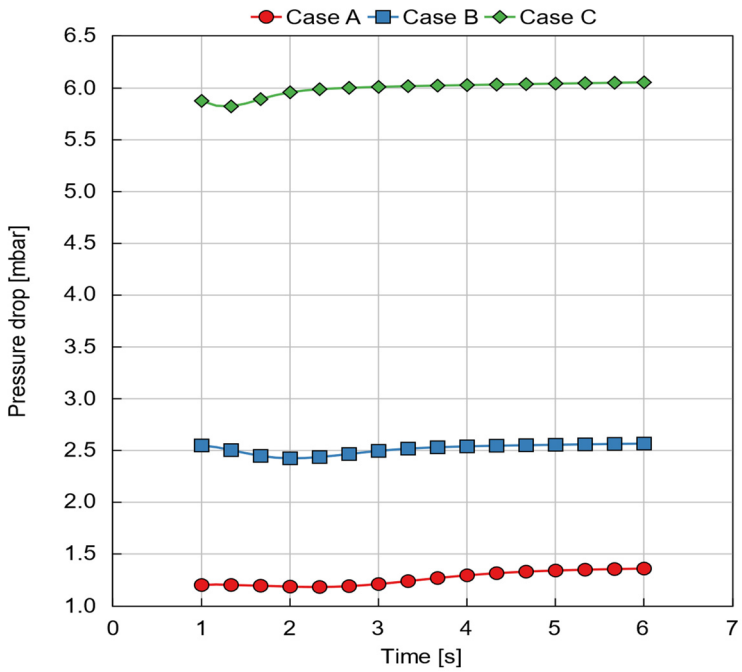

Figure 18. Pressure drop in catalyst brick for three engine operating points.

4.7. Sensitivity of MOC's Geometrical Parameters

The findings concerning conversion efficiency, temperature, and pressure drop indicate that the three engine-load case scenarios exhibited different trends in conversion efficiency and thermal and pressure management. A geometry sensitivity analysis has been carried out for all three cases. It was conducted on catalysts of three different lengths—300 mm, 400 mm, and 500 mm. Each length was swept across cell densities ranging from the baseline 2 (1/cm^2) to 20 (1/cm^2). The analysis considered conversion efficiency, pressure drop, inlet temperature, and simulated engine efficiency, aiming to select the best catalyst geometry.

Figure 17 shows these quantities at the low-load operating point (Case A). It shows that THC conversion efficiency exceeds 60% for all catalyst lengths and cell densities, almost reaching 100% for cell densities above 15 (1/cm^2). Although the pressure drop (Figure 17c) remains within an acceptable range at these higher cell densities, the catalyst inlet temperature falls below its 500 K light-off limit when the baseline brick length of 300 mm is considered. Although Figure 17b indicates that temperature does not significantly impact THC conversion, this decrease may pose a problem at the low-load operating point [28,32]. The light-off limit was reached between 10 and 12 cells/cm^2 for the two longer catalysts. The limitation in terms of inlet temperature is depicted by the yellow area; the threshold limitation for the minimum THC efficiency of 70% is depicted by the yellow area in Figure 17a.

Backpressure increased the pumping work of the engine, so even the least dense and shortest catalyst exerted an indicated efficiency penalty of 2.1%. The penalty increased to 2.65% for the 500 mm long catalyst with the highest density (Figure 17d). However, this efficiency deterioration was considered acceptable. Regarding the limitations arising from inlet temperature and THC conversion efficiency, depicted by the yellow areas, a cell density between 3 and 10 (1/cm^2) seems feasible for all considered catalyst lengths.

Figure 19 applies the same criteria to assess the mid-load scenario, Case B. Figure 19a shows that the THC conversion efficiency threshold of 70% was achieved with a minimum catalyst length of 300 mm and a cell density of 4 (1/cm^2). The efficiency could exceed 80% if the same cell density was used in the two longer catalysts. Figure 19b shows that there was a moderate temperature drop with longer catalysts and a greater cell density, but it remained above 500 K. Equally, indicated efficiency penalty rose but was still below 3% in all cases (Figure 19d). One should note that the penalty in the single-cylinder model (without

turbocharger) was attributed almost exclusively to higher pumping losses and should be treated as indicative only. Increased backpressure in an actual engine usually causes the turbocharger to operate at a more efficient operating point of the map. Turbocharger tuning can effectively reduce the penalty to less than 2% per 0.1 bar of increased backpressure [47].

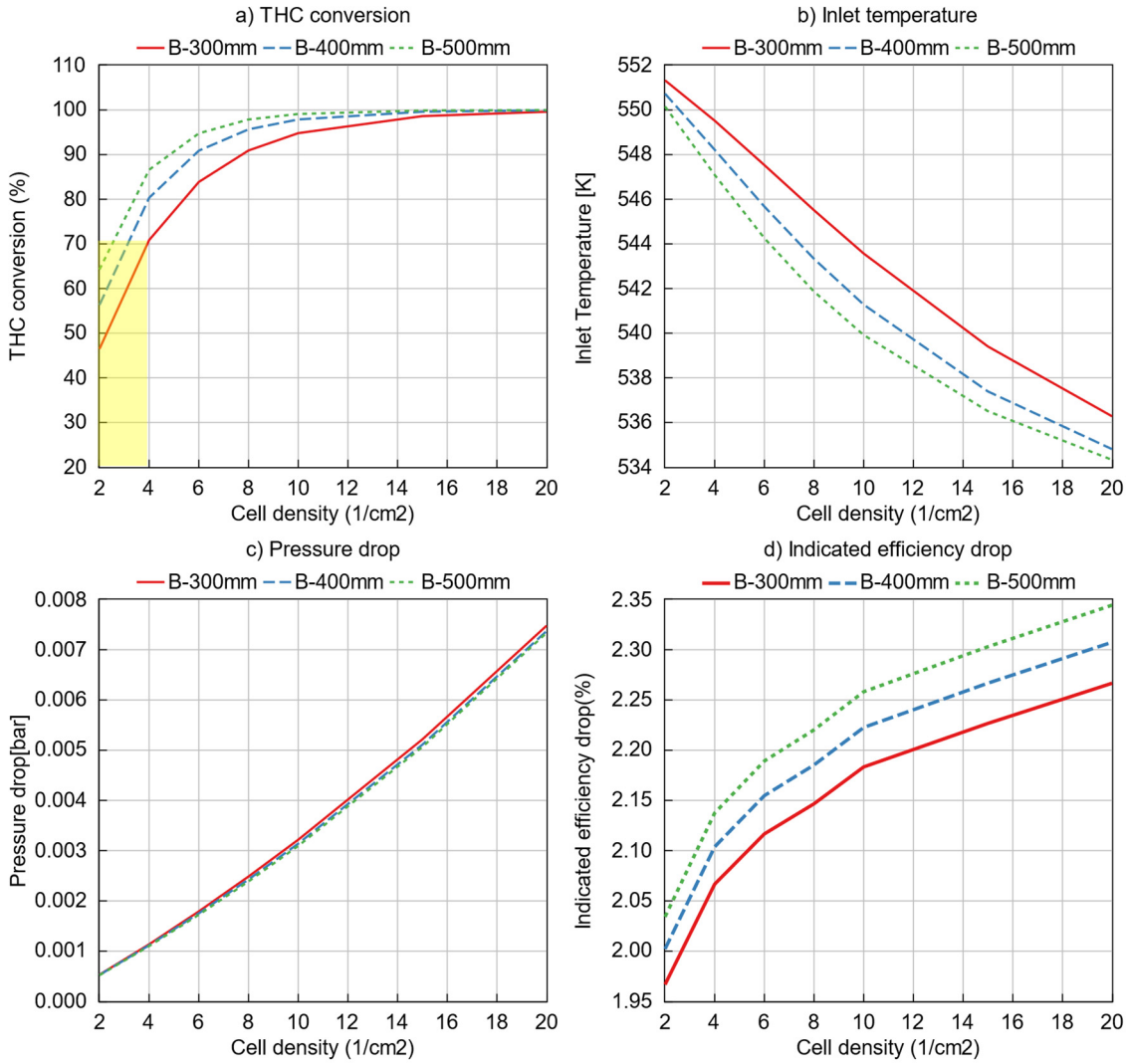

Figure 19. (**a**) THC conversion; (**b**) catalyst inlet temperature; (**c**) pressure drop; (**d**) indicated efficiency drop for mid-load case (Case B) in various geometries and cell densities, yellow area illustrated un-desired domain.

Comparing the criteria for indicated efficiency penalty, the high-load case (Figure 20d) demonstrated a more favourable scenario than the mid-load condition. As illustrated in Figure 20d, the maximum efficiency drop was 2.9%, applicable to the longest catalyst with a high cell density. The 70% THC conversion rate was feasible in the high-load scenario for a 300 mm long catalyst with a cell density of 7 ($1/cm^2$), as depicted in Figure 20a. This same 70% minimum conversion threshold with 400 mm and 500 mm long catalysts was reached at cell densities of 5 ($1/cm^2$) and 4 ($1/cm^2$), respectively.

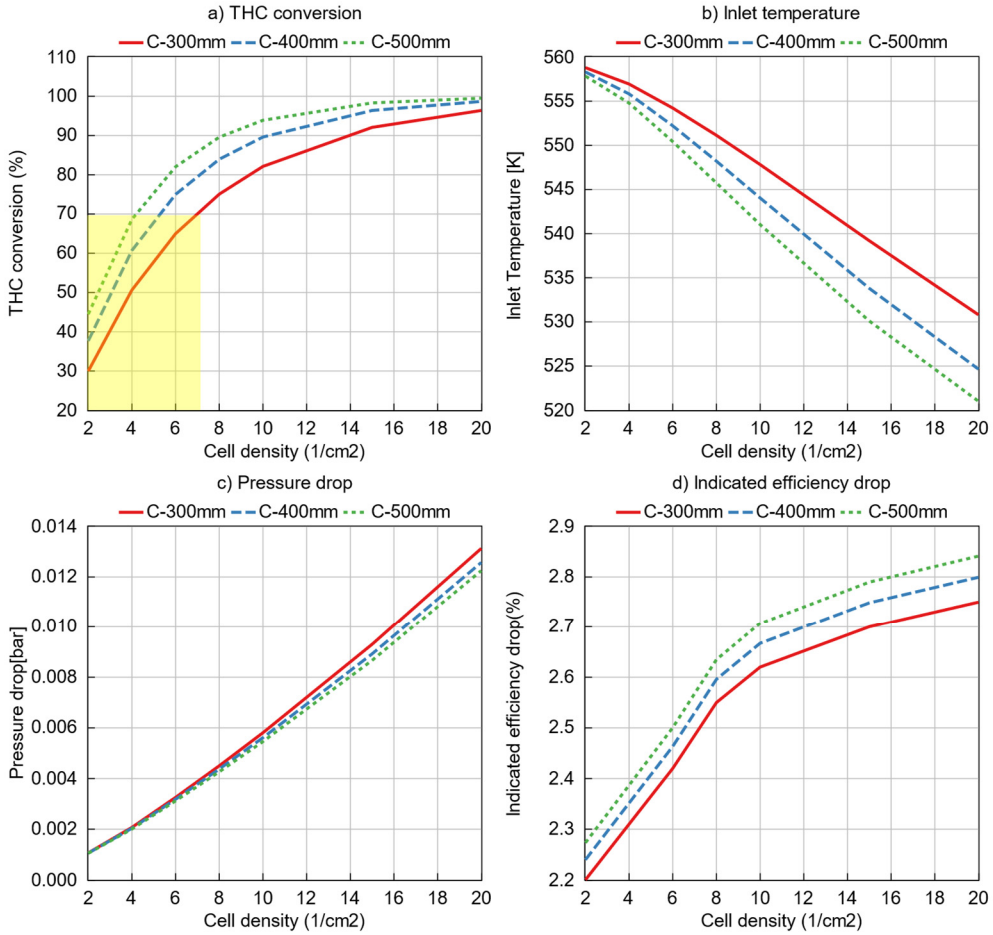

Figure 20. (**a**) THC conversion; (**b**) catalyst inlet temperature; (**c**) pressure drop; and (**d**) indicated efficiency drop for high-load case (Case C) in various geometries and cell densities, yellow area illustrated un-desired domain.

Weighing the above geometrical considerations against commercially available MOCs gave additional insight into the technological constraints. A chosen typical heavy-duty, on-road MOC, 152 mm long with a diameter of 266 mm, had a mesh density of 600 cells per square inch, equal to 93 cells per cm^2 [48]. The catalysts' lengths in the current study were 300 mm, 400 mm, and 500 mm, each had a 300 mm diameter, and the maximum cell density varied from 40 to 20 ($1/cm^2$). With this selection, the effective area was approximately the same as the commercial MOC catalyst [47] while avoiding the limitations explained for the three case studies. Therefore, a catalyst brick with a length of 400 mm and a cell density of 10 ($1/cm^2$) has been selected for the marine engine application considered in this study.

4.8. Benchmark RCCI with and without MOC

The selected MOC brick configuration (400 mm in length and with cell density of 10 cells/cm^2) has been benchmarked against the RCCI engine without an MOC. Bearing in mind the earlier remarks concerning a turbocharger's effect in mitigating the pumping losses caused by increased backpressure, brake efficiency was obtained by applying the calculated backpressure on the GT-Power model of a corresponding one-cylinder production version of the SCRE considered here for reactive simulation. The model was operated at corresponding load points, with the burn rates imposed from the fully predictive SCRE simulations. As previously highlighted, the model involved a BMEP and lambda controller to ensure that both cases were simulated at the same calibration, despite different boundary pressures. With the above assumptions, Figure 21 compares the results of the RCCI engine, with and without an MOC.

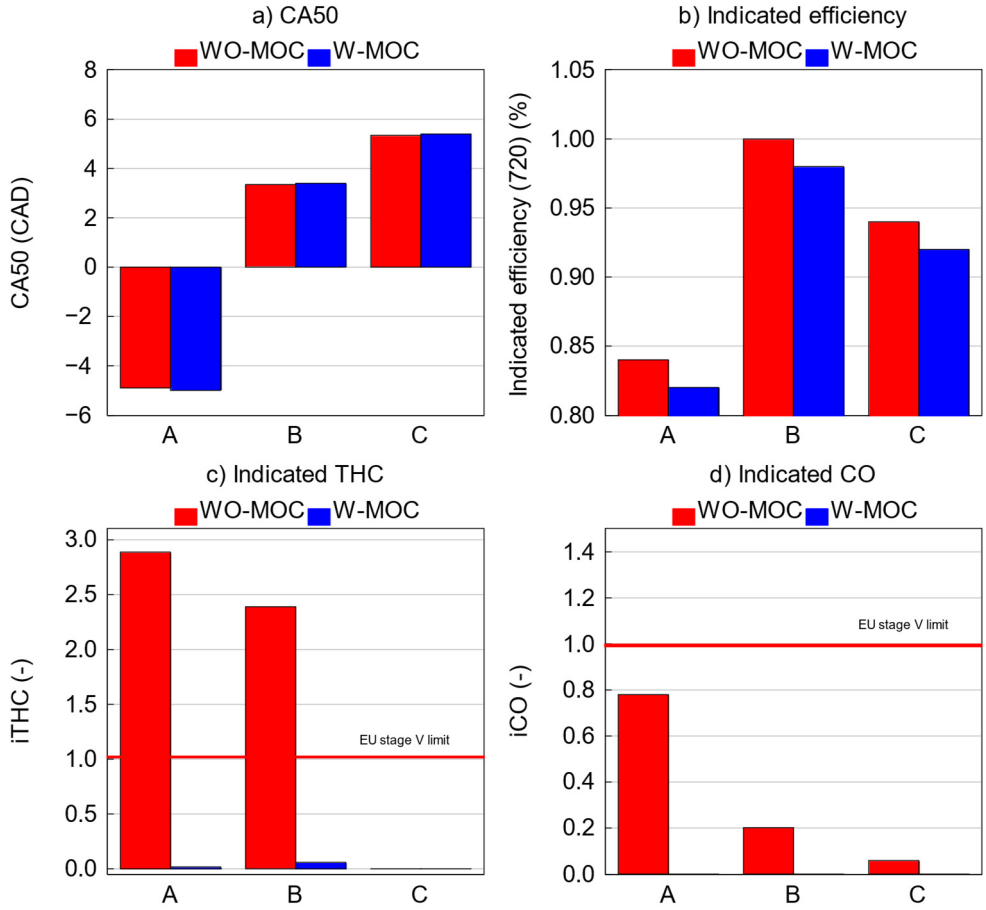

Figure 21. (**a**) CA50; (**b**) indicated efficiency (720 degrees); (**c**) indicated total number of hydrocarbons; and (**d**) indicated CO. Normalised depiction.

The main difference became apparent in the 720 degree, gross indicated efficiency. Figure 21b illustrates this change by comparing gross indicated efficiency across all three engine loads in both engine air-path models. All quantities have been normalised with the mid-load case efficiency without a catalyst (WO-MOC). The efficiency is reduced by around 2% for all cases with a catalyst (W-MOC).

Figure 21a depicts CA50, revealing negligible differences across all three engine-loads.

The benefits of employing the MOC manifest in significantly reduced emissions, as depicted in Figure 21c,d. This figure provides indicated specific emissions of THC and CO in both W-MOC and WO-MOC air-path models. The quantities have been normalised with iTHC and iCO thresholds in EU Stage V limits. Substantial reductions in both iTHC and iCO emissions with the catalyst are evident in all three cases. CO emissions in the W-MOC scenario register at zero for all engine loads (Figure 21d).

Indicated total hydrocarbons emissions (iTHC) without the catalyst exhibited values above the threshold in the low- and mid-load cases (Figure 21c). Integration of the MOC reduced these values well below EU Stage V limits. It is noteworthy that the elevated temperature in the high-load scenarios resulted in considerably lower THC emissions compared to in other cases.

5. Conclusions

This study highlighted the efficacy of advanced kinetic-based combustion models for comprehensive engine and aftertreatment simulations. It demonstrated that a coupled multizone model with detailed reaction kinetics and aftertreatment integration can converge in under 12 s for steady-state simulations. Convergence times can vary based on initial conditions and combustion variability. This research study also found that the model

accurately captured the impact of aftertreatment-induced backpressure on combustion. Despite the simulation running at a speed of three minutes per cycle—slightly slower than a standalone combustion model—it achieved high accuracy within a 5% error margin for performance metrics and emissions.

Moreover, this study underscored the critical role of hydrogen in driving the spontaneity of methane reactions and the importance of oxygen in catalytic processes.

The analysis of catalyst brick geometries identified a 400 mm long oxidation reactor with a cell density of 10 ($1/cm^2$) as optimal, achieving significant hydrocarbon conversion rates and maintaining an acceptable pressure drop below 0.1 bar, thus offering flexibility in design. However, the introduction of aftertreatment systems was found to compromise engine performance, with efficiency penalties ranging between 2.45% and 2.65% across different load points; while more than 98% of carbon oxides were converted, unburned hydrocarbon reduction was about 70%.

Moving forward, it has been planned to make the developed UVATZ RCCI model faster and to improve its predictive capability. Our step-by-step approach to adding more details to the model helps to prepare a detailed and accurate engine model which has high accuracy in predicting combustion and emission specifications considering the effectiveness of various engine system parts such as various types of aftertreatments, turbochargers, etc.

Author Contributions: Conceptualization, M.M. and A.K.; methodology, M.M. and A.K.; software, A.K.; validation, A.K. and M.M.; formal analysis, A.K.; investigation; A.K., J.H. and M.M.; resources, M.M.; data curation, A.K.; writing—original draft preparation, A.K.; writing—review and editing, A.K., J.H. and M.M.; visualization, M.M. and J.H.; supervision, M.M.; project administration, M.M.; funding acquisition, M.M. All authors have read and agreed to the published version of the manuscript.

Funding: The work was conducted in the framework of the Clean Propulsion Technologies project with financial support from Business Finland (ref. 38475/31/2020).

Institutional Review Board Statement: Not available.

Informed Consent Statement: Not available.

Data Availability Statement: Data is contained within the article.

Conflicts of Interest: The authors declare no conflict of interest.

Nomenclature

A/F	air/fuel
AFR	air flow rate
BR	blend ratio
BSAC	brake-specific air consumption
BSFC	brake-specific fuel consumption
BTE	brake thermal efficiency
CAD	crank angle degree
CAX	crank angle corresponding to X% energy released
CFD	computational fluid dynamics
CHR	cumulative heat release
CMP	compression
DOC	diesel oxidiser catalyst
EGR	exhaust gas recirculation
EXH	exhaust
EATS	engine aftertreatment system
GTP	GT-Power
IMEP	indicated mean effective pressure
IMO	International Maritime Organization
IP	indicated power
ISAC	indicated specific air consumption

ISFC	indicated specific fuel consumption
ITE	indicated thermal efficiency
IVC	intake valve closing
LFO	light fuel oil
LTC	low-temperature combustion
MN	methane number
MOC	methane oxidiser catalyst
MZM	multizone model
NG	natural gas
NHR	net heat released
OEMs	original equipment manufacturers
PGM	platinum group metal
pp	percentage points
PRR	pressure rise rate
PWR	power
RCCI	reactivity-controlled compression ignition
ROHR	rate of heat release
SCRE	single-cylinder research engine
SOC	start of combustion
SOI	start of injection
TDC	top dead centre
TR	trapping ratio
THC	total hydrocarbons
VE	volumetric efficiency
UVATZ	University of Vaasa advanced thermokinetic multizone
	Symbols
P	pressure
Pt	platinum
Pd	palladium
Rh	rhodium
P_{max}	maximum pressure
T	temperature
λ	air–fuel equivalence ratio
ζ_t	interzonal mixing intensity
ζ_∇	gradient of high-reactivity fuel stratification

Appendix A. Reaction Matrix and Thermodynamic Analysis

The main text determined that the most abundant reactive NG–diesel RCCI engine exhaust species were H_2, H_2O, CO_2, CO, CH_4, C_2H_6, C_2H_4, and O_2. They were considered for the catalytic reactions study; possible reactions involving these species have been listed in Table A1 [49]. The table shown the activation energy for each reaction, indicating whether the reactions can occur spontaneously or not. If not, the reactions were facilitated by the presence of other species. Specifically, the majority of reactions occurred spontaneously when there was sufficient hydrogen in the exhaust gas. However, in the absence of hydrogen, the direction of the reactions could be altered. Obviously, oxygen was the most significant species in the oxidation reaction matrices R2, R9, R13, and R15.

One noteworthy reaction is R6, known as the Boudouard reaction. This was particularly important due to possible production of soot outside of the engine cylinder. This reaction was spontaneous and exothermic at all temperatures but requires elevated temperatures to occur. In addition to the Boudouard reaction, the water–gas shift reactions R10 and R11 played a crucial role in soot production. Both required the presence of hydrogen, which can be supplied through another water–gas shift reaction, R7.

Table A1. Possible reactions for system of species [49].

	Reaction	$\Delta H\left(\frac{kJ}{mol}\right)$	Reaction Type
R1	$CO + 3H_2 \leftrightarrow CH_4 + H_2O$	**−206.1**	CO methanation
R2	$CO + 0.5O_2 \leftrightarrow CO_2$	**−283**	CO oxidation
R3	$CO_2 + 4H_2 \leftrightarrow CH_4 + 2H_2O$	**−165.0**	CO_2 methanation
R4	$2CO + 2H_2 \leftrightarrow CH_4 + CO_2$	**−247.3**	Inverse methane CO_2 reform
R5	$CH_4 + 2O_2 \leftrightarrow CO_2 + 2H_2O$	**−802**	Water–methane shift
R6	$2CO \leftrightarrow C + CO_2$	**−172.4**	Boudouard reaction
R7	$CO + H_2O \leftrightarrow CO_2 + H_2$	**−41.2**	Water–gas shift
R8	$CH_4 \leftrightarrow 2H_2 + C$	**+74.8**	Methane cracking
R9	$H_2 + 0.5O_2 \leftrightarrow H_2O$	**−241**	H_2 burning
R10	$CO + H_2 \leftrightarrow C + H_2O$	**−131.3**	Carbon moNOxide reduction
R11	$CO_2 + 2H_2 \leftrightarrow C + 2H_2O$	**−90.1**	Carbon dioxide reduction
R12	$C_2H_6 + 2H_2O \leftrightarrow 2CO + 5H_2$	**+340**	Ethane conversion to CO
R13	$C_2H_6 + 3.5O_2 \leftrightarrow 2CO_2 + 3H_2O$	**−1434**	Ethane oxidation
R14	$C_2H_4 + 2H_2O \leftrightarrow 2CO_2 + 4H_2$	**+210**	Ethylene conversion to CO_2
R15	$C_2H_4 + 3O_2 \leftrightarrow 2CO_2 + 2H_2O$	**−1322**	Ethylene oxidation

Figure A1 depicted the spontaneous behaviour of various reactions. It shown that oxidation reactions R5, R13, and R15 were highly spontaneous and occur rapidly, converting hydrocarbons directly into final products. One should note that these three reactions did not occur in the absence of oxygen in the exhaust gas, for example in fuel-rich conditions. All other reactions were observed to be exothermic and spontaneous, except for methane cracking (R8), ethane–water (R12), and ethylene–water (R14) reactions, which required activation energy to occur. These three reactions were spontaneous in the reverse direction.

Hydrogen played a crucial role in this reaction matrix. With an abundance of hydrogen, reactions R1, R3, R4, R7, R9, R10, R11, and R8 occur in forward direction, and R12 and R14 occur in the reverse direction. Therefore, hydrogen concentration was a key controller of these reactions. Hydrogen can be supplied by the water–gas shift reaction (R7), which is both spontaneous and exothermic.

Examination of the available species and the potential reactions in Table A1, and of the equilibrium constants in Figure A1, explained the inhibitory roles of various species. The main combustion products CO_2 and H_2O played inhibitory roles in the oxidation of three main hydrocarbons (R13, R15, and R5) by increasing the concentration of products. Even though CO did not directly contribute to oxidation reactions, it was converted to CO_2 via a spontaneous reaction (R2) with an excess of oxygen, further enhancing its inhibitory effect. The water–gas shift reaction (R7), which was also spontaneous, increased the inhibitory role of CO and H_2O while producing H_2. In turn, with the presence of CO and CO_2, hydrogen participated in reactions R1 and reverse reactions R12 and R14, yielding methane, ethane, and ethylene. Reaction R6, followed by reversed reaction R8, showed another inhibitory role of CO. Finally, it can be stated that CO, H_2O, and CO_2 were the main inhibitory species in methane removal from the exhaust. These inhibitory mechanisms should be considered when choosing an appropriate aftertreatment catalyst.

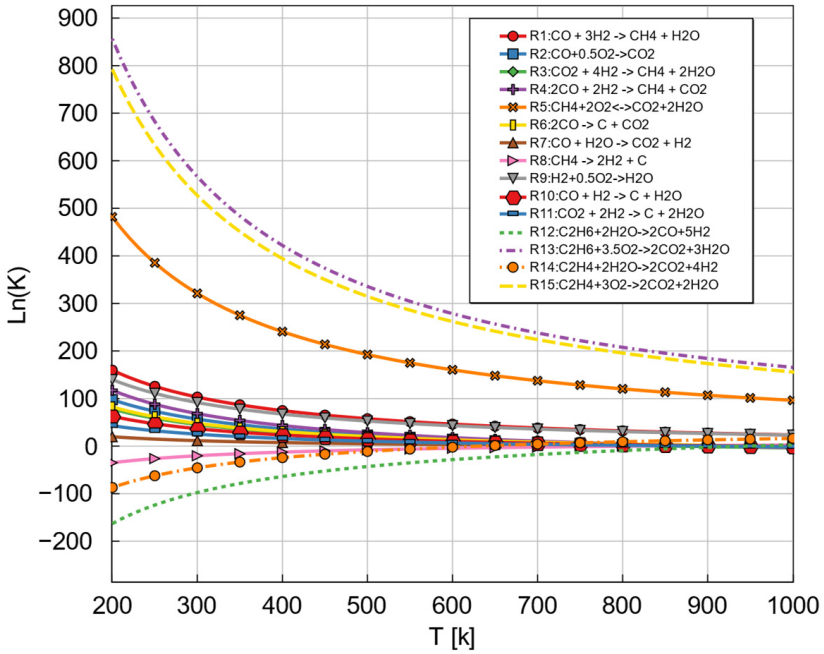

Figure A1. Logarithmic equilibrium constant of various possible reactions.

The engine exhaust valve temperature and pressure in this study were approximately 550 K and 5 bar, respectively. This temperature prompted analysis of other possible species, using the same analysis as A. Kakoee et al. [37] involving the Gibbs equation. Figure A2 depicts the concentrations of various species.

H_2O, CO_2, CO, CH_4, C_2H_4, and C_2H_6 were considered species at equilibrium with the mentioned possible reactions. In this analysis, equilibrium referred to the amount of the mole fraction of mentioned species at each pressure and temperature. The initial values for these species were selected as follows: 1, 0.5, 0.18, 0.05, 0.014, and 0.0033, respectively, for H_2O, CO_2, CO, CH_4, C_2H_4, and C_2H_6. The pressure of the system of reactions was 5 bar. H_2O and CO_2 are the most bolded species according to their concentrations. According to this figure, as mentioned soot emissions were possible with the presence of C that can be released from R6, the Boudouard reaction, a spontaneous reaction. The concentrations of C and C_2H_6 were approximately the same due to chemical equilibrium. The Boudouard reaction was a spontaneous reaction that completely consumes the output CO and converted it to mainly CO2 and C. Although the initial mixture did not contain hydrogen, its concentration increased from approximately 350 K. This phenomenon can cause the occurrence of all of those reactions in the presence of this species, as tabulated in Table A1. As depicted in the Figure A2, CH_4 completely converted at 800 K. Around this temperature, a turning point occurred for approximately all species. The depicted concentrations were the final outputs of the species with 15 possible reactions before going through the aftertreatment system.

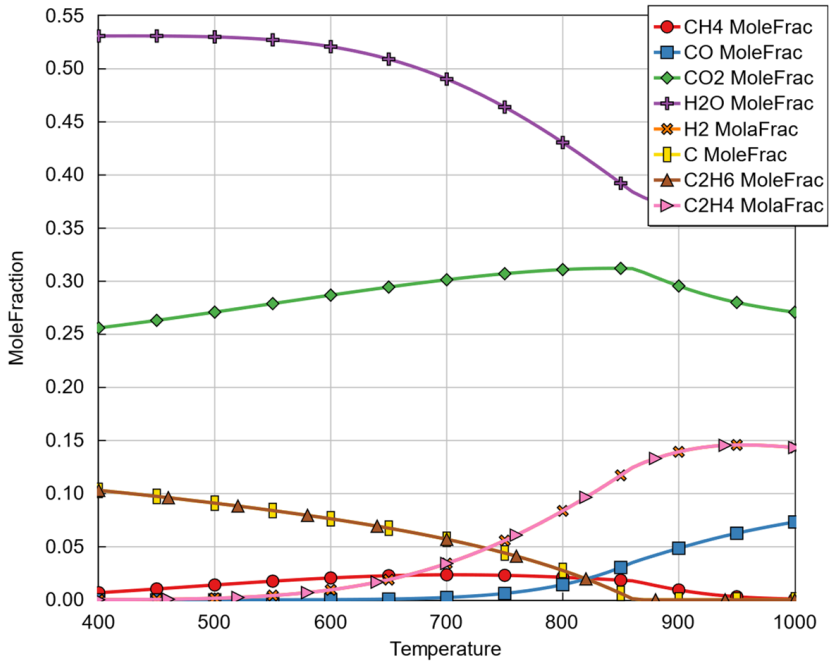

Figure A2. Possible species' mole fractions in exhaust air path at various temperatures and pressures.

References

1. Ni, P.; Wang, X.; Li, H. A review on regulations, current status, effects and reduction strategies of emissions for marine diesel engines. *Fuel* **2020**, *279*, 118477. [CrossRef]
2. Wärtsilä. Power Plants Solutions. n.d. Available online: https://cdn.wartsila.com/docs/default-source/power-plants-documents/ppscatalog_lowres_030616_56mt.pdf?sfvrsn=e5b3dc45_2 (accessed on 1 January 2021).
3. MAN. Energy Solutions. n.d. Available online: https://www.man-es.com/ (accessed on 1 January 2020).
4. Mikulski, M.; Ramesh, S.; Bekdemir, C. Reactivity Controlled Compression Ignition for clean and efficient ship propulsion. *Energy* **2019**, *182*, 1173–1192. [CrossRef]
5. Hautala, S.; Mikulski, M.; Söderäng, E.; Storm, X.; Niemi, S. Toward a digital twin of a mid-speed marine engine: From detailed 1D engine model to real-time implementation on a target platform. *Int. J. Engine Res.* **2022**, *24*, 4553–4571. [CrossRef]
6. Mikulski, M.; Balakrishnan, P.R.; Hunicz, J. Natural gas-diesel reactivity controlled compression ignition with negative valve overlap and in-cylinder fuel reforming. *Appl. Energy* **2019**, *254*, 113638. [CrossRef]
7. Elumalai, R.; Ravi, K. Strategy to reduce carbon emissions by adopting ammonia–Algal biodiesel in RCCI engine and optimize the fuel concoction using RSM methodology. *Int. J. Hydrogen Energy* **2022**, *47*, 39701–39718. [CrossRef]
8. Zhang, R.; Chen, L.; Wei, H.; Li, J.; Ding, Y.; Chen, R.; Pan, J. Experimental investigation on reactivity-controlled compression ignition (RCCI) combustion characteristic of n-heptane/ammonia based on an optical engine. *Int. J. Engine Res.* **2023**, *24*, 2478–2488. [CrossRef]
9. Kakoee, A.; Gharehghani, A. Comparative study of hydrogen addition effects on the natural-gas/diesel and natural-gas/dimethyl-ether reactivity controlled compression ignition mode of operation. *Energy Convers. Manag.* **2019**, *196*, 92–104. [CrossRef]
10. Kakoee, A.; Bakhshan, Y.; Aval, S.M.; Gharehghani, A. An improvement of a lean burning condition of natural gas/diesel RCCI engine with a pre-chamber by using hydrogen. *Energy Convers. Manag.* **2018**, *166*, 489–499. [CrossRef]
11. Benajes, J.; García, A.; Monsalve-Serrano, J.; Lago Sari, R. Fuel consumption and engine-out emissions estimations of a light-duty engine running in dual-mode RCCI/CDC with different fuels and driving cycles. *Energy* **2018**, *157*, 19–30. [CrossRef]
12. Kokjohn, S.L.; Hanson, R.M.; Splitter, D.A.; Reitz, R.D. Experiments and Modeling of Dual-Fuel HCCI and PCCI Combustion Using In-Cylinder Fuel Blending. *SAE Int. J. Engines* **2009**, *2*, 24–39. [CrossRef]
13. Hanson, R.M.; Kokjohn, S.L.; Splitter, D.A.; Reitz, R.D. An Experimental Investigation of Fuel Reactivity Controlled PCCI Combustion in a Heavy-Duty Engine. *SAE Int. J. Engines* **2010**, *3*, 700–716. [CrossRef]
14. Pedrozo, V.B.; Wang, X.; Guan, W.; Zhao, H. The effects of natural gas composition on conventional dual-fuel and reactivity-controlled compression ignition combustion in a heavy-duty diesel engine. *Int. J. Engine Res.* **2022**, *23*, 397–415. [CrossRef]
15. Piqueras, P.; García, A.; Monsalve-Serrano, J.; Ruiz, M.J. Performance of a diesel oxidation catalyst under diesel-gasoline reactivity controlled compression ignition combustion conditions. *Energy Convers. Manag.* **2019**, *196*, 18–31. [CrossRef]
16. Mortensen, R.L.; Noack, H.; Pedersen, K.; Mossin, S.; Mielby, J. Recent Advances in Complete Methane Oxidation using Zeolite-Supported Metal Nanoparticle Catalysts. *ChemCatChem* **2022**, *14*, e202101924. [CrossRef]

17. Xu, G.; Jia, M.; Li, Y.; Chang, Y.; Liu, H.; Wang, T. Evaluation of variable compression ratio (VCR) and variable valve timing (VVT) strategies in a heavy-duty diesel engine with reactivity controlled compression ignition (RCCI) combustion under a wide load range. *Fuel* **2019**, *253*, 114–128. [CrossRef]
18. Xu, G.; Jia, M.; Li, Y.; Chang, Y.; Wang, T. Potential of reactivity controlled compression ignition (RCCI) combustion coupled with variable valve timing (VVT) strategy for meeting Euro 6 emission regulations and high fuel efficiency in a heavy-duty diesel engine. *Energy Convers. Manag.* **2018**, *171*, 683–698. [CrossRef]
19. Herreros, J.M.; Gill, S.S.; Lefort, I.; Tsolakis, A.; Millington, P.; Moss, E. Enhancing the low temperature oxidation performance over a Pt and a Pt–Pd diesel oxidation catalyst. *Appl. Catal. B Environ.* **2014**, *147*, 835–841. [CrossRef]
20. Xie, L.; Jiang, G.; Qian, F. Research on Aftertreatment Inlet_Outlet Insulation for a Nonroad Middle Range Diesel Engine. *Catalysts* **2020**, *10*, 454. [CrossRef]
21. Tsuchiya, A.; Masaoka, S.; Ohyama, J.; Sawabe, K.; Satsuma, A. Effects of carbon number and bond saturation on hydrocarbon combustion over a diesel oxidation catalyst. *Catal. Sci. Technol.* **2020**, *10*, 3868–3874. [CrossRef]
22. Gao, J.; Tian, G.; Sorniotti, A.; Karci, A.E.; Di Palo, R. Review of thermal management of catalytic converters to decrease engine emissions during cold start and warm up. *Appl. Therm. Eng.* **2019**, *147*, 177–187. [CrossRef]
23. Hasan, A.O.; Abu-Jrai, A.; Al-Muhtaseb, A.H.; Tsolakis, A.; Xu, H. HC, CO and NOx emissions reduction efficiency of a prototype catalyst in gasoline bi-mode SI/HCCI engine. *J. Environ. Chem. Eng.* **2016**, *4*, 2410–2416. [CrossRef]
24. Hasan, A.O.; Abu-jrai, A.; Al-Muhtaseb, A.H.; Tsolakis, A.; Xu, H. Formaldehyde, acetaldehyde and other aldehyde emissions from HCCI/SI gasoline engine equipped with prototype catalyst. *Fuel* **2016**, *175*, 249–256. [CrossRef]
25. Hasan, A.O.; Leung, P.; Tsolakis, A.; Golunski, S.E.; Xu, H.M.; Wyszynski, M.L.; Richardson, S. Effect of composite aftertreatment catalyst on alkane, alkene and monocyclic aromatic emissions from an HCCI/SI gasoline engine. *Fuel* **2011**, *90*, 1457–1464. [CrossRef]
26. Hunicz, J.; Medina, A. Experimental study on detailed emissions speciation of an HCCI engine equipped with a three-way catalytic converter. *Energy* **2016**, *117*, 388–397. [CrossRef]
27. Prikhodko, V.Y.; Curran, S.J.; Parks, J.E.; Wagner, R.M. Effectiveness of Diesel Oxidation Catalyst in Reducing HC and CO Emissions from Reactivity Controlled Compression Ignition. *SAE Int. J. Fuels Lubr.* **2013**, *6*, 329–335. [CrossRef]
28. Stakheev, A.Y.; Batkin, A.M.; Teleguina, N.S.; Bragina, G.O.; Zaikovsky, V.I.; Prosvirin, I.P.; Khudorozhkov, A.K.; Bukhtiyarov, V.I. Particle Size Effect on CH4 Oxidation Over Noble Metals: Comparison of Pt and Pd Catalysts. *Top. Catal.* **2013**, *56*, 306–310. [CrossRef]
29. Ottinger, N.; Veele, R.; Xi, Y.; Liu, Z.G. Desulfation of Pd-based Oxidation Catalysts for Lean-burn Natural Gas and Dual-fuel Applications. *SAE Int. J. Engines* **2015**, *8*, 1472–1477. [CrossRef]
30. Lehtoranta, K.; Koponen, P.; Vesala, H.; Kallinen, K.; Maunula, T. Performance and Regeneration of Methane Oxidation Catalyst for LNG Ships. *JMSE* **2021**, *9*, 111. [CrossRef]
31. Heikkilä, S.; Sirviö, K.; Niemi, S.; Roslund, P.; Lehtoranta, K.; Pettinen, R.; Vesala, H.; Koponen, P.; Kallinen, K.; Maunula, T.; et al. Methane Catalyst Regeneration with Hydrogen Addition. In Proceedings of the Future of Combustion Engines: 29th CIMAC World Congress, Vancouver, BC, Canada, 10–14 June 2019. Article 367.
32. Tziolas, V.; Koltsakis, G.; Chatzipartali, K. *Coupled Engine and after-Treatment Simulation for Fuel Efficient EU7 Technologies*; Technical Paper 2023-24-0104; SAE International: Capri, Italy, 2023. [CrossRef]
33. Leon de Syniawa, L.; Siddareddy, R.B.; Oder, J.; Franken, T.; Guenther, V.; Rottengruber, H.; Mauss, F. *Real-Time Simulation of CNG Engine and after-Treatment System Cold Start. Part 2: Tail-Pipe Emissions Prediction Using a Detailed Chemistry Based MOC Model*; Technical Paper 2023-01-0364; SAE International: Detroit, MI, USA, 2023. [CrossRef]
34. Kakoee, A.; Vasudev, A.; Smulter, B.; Hyvonen, J.; Mikulski, M. *A Predictive 1D Modeling Framework for Reactivity-Controlled Compression Ignition Engines, via a Chemistry-Based, Multizone Combustion Object*; SAE International: Capri, Italy, 2023; p. 11.
35. Vasudev, A.; Mikulski, M.; Balakrishnan, P.R.; Storm, X.; Hunicz, J. Thermo-kinetic multi-zone modelling of low temperature combustion engines. *Prog. Energy Combust. Sci.* **2022**, *91*, 100998. [CrossRef]
36. Gamma Technologies. *GT-Suite Overview*; Gamma Technologies: Westmont, IL, USA, 2022.
37. Khosravi, M.; Abedi, A.; Hayes, R.E.; Epling, W.S.; Votsmeier, M. Kinetic modelling of Pt and Pt:Pd diesel oxidation catalysts. *Appl. Catal. B Environ.* **2014**, *154–155*, 16–26. [CrossRef]
38. Jay, D. CR development in the last decade in Wärtsilä. In Proceedings of the 28th CIMAC World Congress, Helsinky, Finland, 6–10 June 2016; pp. 6–10.
39. GT Suite. *Engine Performance Application Manual*; Gamma Technologies: Westmont, IL, USA, 2023.
40. Chang, J.; Güralp, O.; Filipi, Z.; Assanis, D.; Kuo, T.-W.; Najt, P.; Rask, R. New Heat Transfer Correlation for an HCCI Engine Derived from Measurements of Instantaneous Surface Heat Flux. *SAE Int.* **2004**, *113*, 1576–1593.
41. Yang, J.; Martin, J.K. Approximate Solution—One-Dimensional Energy Equation for Transient, Compressible, Low Mach Number Turbulent Boundary Layer Flows. *J. Heat. Transf.* **1989**, *111*, 619–624. [CrossRef]
42. Yao, T.; Pei, Y.; Zhong, B.-J.; Som, S.; Lu, T.; Luo, K.H. A compact skeletal mechanism for n-dodecane with optimized semi-global low-temperature chemistry for diesel engine simulations. *Fuel* **2017**, *191*, 339–349. [CrossRef]
43. Fayyazbakhsh, A.; Bell, M.L.; Zhu, X.; Mei, X.; Koutný, M.; Hajinajaf, N.; Zhang, Y. Engine emissions with air pollutants and greenhouse gases and their control technologies. *J. Clean. Prod.* **2022**, *376*, 134260. [CrossRef]
44. Joshi, A. Review of Vehicle Engine Efficiency and Emissions. *SAE Int. J. Adv. Curr. Pract. Mobil.* **2020**, *2*, 2479–2507. [CrossRef]

45. Sampara, C.S.; Bissett, E.J.; Assanis, D. Hydrocarbon storage modeling for diesel oxidation catalysts. *Chem. Eng. Sci.* **2008**, *63*, 5179–5192. [CrossRef]
46. Bermúdez, V.; Serrano, J.R.; Piqueras, P.; García-Afonso, O. Pre-DPF water injection technique for pressure drop control in loaded wall-flow diesel particulate filters. *Appl. Energy* **2015**, *140*, 234–245. [CrossRef]
47. Kim, J.; Chiong, M.S.; Rajoo, S. Effect of Turbine Upstream Geometry on Pulsating Flow and Turbocharged Si-Engine Perfor-mance. *Int. J. Automot. Technol.* **2023**, *24*, 527–539. [CrossRef]
48. Sinocat Environmental Technology Co., Ltd. Available online: http://en.sinocat.com.cn/ (accessed on 1 January 2019).
49. Kakoee, A.; Gharehghani, A. Carbon oxides methanation in equilibrium; a thermodynamic approach. *Int. J. Hydrogen Energy* **2020**, *45*, 29993–30008. [CrossRef]